Stellar kinematics in the Large Magellanic Cloud

Lisa Di Carlo

A thesis submitted for the degree of
Master of Science in **Astrophysics**
at the **University of Potsdam**

Supervised by:

Prof. Dr. Maria-Rosa Cioni

Alla mia fortissima nonna,
la mia fan numero uno.
Ti voglio bene e te ne vorrò sempre.

Acknowledgements

I would like to begin by expressing my sincere gratitude to my thesis supervisor *Prof. Dr. Maria-Rosa Cioni*, first and foremost for her guidance, wisdom, and scientific expertise, but also for her patience, humanity, and kindness that she showed me throughout these past years. I would like to thank *Dr. Nikolay Kacharov* for his help with the coding part of the thesis, in particular for the analysis and processing of the spectra. In addition, I wish to acknowledge *Dr. Dalal El Youssoufi*, whose work on the Small Magellanic Cloud inspired this project; her studies on the Clouds were extremely helpful, especially for the introduction of this work.
I'd also like to extend my thanks to *Prof. Dr. Katja Poppenhäger* for kindly agreeing to serve as second reader of this thesis and for her time and attention.

To my amazing partner, *Andrea*, who has always stood by my side, always believed in me, and most importantly, always reminded me to believe in myself. Finding you was the luckiest thing that has happened to me.
I am deeply thankful to my family. My father *Luca*, who made all of this possible: I know you hadn't really a choice, but thanks for giving me the opportunity to move away and live my life the way I wanted to; my siblings *Giulia & Pietro*, and my cousins *Elena & Nina*, for shaping the person that I am today: even though we live kilometers apart and do not see each other very often, I love you all very much, and I am really glad to have grown up with you.

Thanks to all the amazing people I've met during my years in Potsdam, my colleagues and my friends. Special thanks to *Charlotte, Geet, Amanda, Karina, Dani, & Nesli*, who have supported me, laughed with me, and kept me going through the ups and downs of this journey. I would also like to thank all of my friends from Pescara, in particular *Flavia, Anna, & Giovanna*, whom I miss very much. You have always reminded me of where I come from and have given me a place to return to, no matter how far I go.

E per ultimo, ma non per importanza, un ringraziamento speciale va a mia madre *Maria Elena*, che non capisce l'inglese. Senza di te, i tuoi sforzi, i tuoi sacrifici, tutte le volte in cui mi hai chiesto ”Quando ti laurei?”, non sarei qui oggi. Grazie per non avermi mai fatto mancare nulla.

Abstract

The Large Magellanic Cloud is the fourth-closest galaxy to us and, together with its companion, the Small Magellanic Cloud, it provides an excellent laboratory for studies of both galaxy interactions and stellar populations. In this thesis, I made use of near-infrared photometry from the Visible and Infrared Survey Telescope for Astronomy and spectra from the Fiber Large Array Multi Element Spectrograph installed at the Very Large Telescope to study the radial velocities of a sample of $\sim$ 4000 Large Magellanic Cloud stars, after performing sky subtraction to clean the spectra, followed by full spectrum fitting using the penalized pixel fitting routine. I derived a mean radial velocity of 273 ± 1 km s^{-1}, and a velocity dispersion of $\sigma_V = 31 \pm 1$ km s^{-1}. The spatial distribution of the velocities is consistent with the known rotation of the LMC disk, with stars on the receding side of the galaxy exhibiting higher velocities. To investigate how radial velocities may vary among stellar populations of different ages, the color–magnitude diagram is divided into regions corresponding to stars at distinct evolutionary stages. One region, encompassing young ($\sim$ 20 Myr) main sequence stars, has a mean velocity of 291 km s^{-1} and stands out clearly against the 265–285 km s^{-1} range of the other regions. The majority of its high-velocity stars lie in the known star-forming region Shapley Constellation III. It is plausible that these stars formed from a dynamically accelerated gas cloud, and they inherited its velocity. The second-youngest region, which hosts main sequence stars of slightly older age, shows the lowest mean radial velocity in the sample and little spatial overlap with Shapley Constellation III. A few stars in this area exhibit low velocities, possibly indicating that they formed before the event that accelerated the gas. Finally, I compare the kinematics of young ($<$ 1 Gyr) and old ($>$ 1 Gyr) populations, finding similar mean velocities (276 ± 1 vs 273 ± 1 km s^{-1}, respectively) and dispersions (31 ± 1 s^{-1} for both).

Zusammenfassung

Die Große Magellansche Wolke ist die viertnächste Galaxie zu uns und bietet zusammen mit ihrer Begleitgalaxie, der Kleinen Magellanschen Wolke, ein ausgezeichnetes Labor für Studien sowohl über Galaxieninteraktionen als auch über stellare Populationen. In dieser Arbeit habe ich nahinfrarote Photometrie vom Visible and Infrared Survey Telescope for Astronomy und Spektren vom Fiber Large Array Multi Element Spectrograph, installiert am Very Large Telescope, verwendet, um die Radialgeschwindigkeiten einer Stichprobe von ~ 4000 Sternen der Großen Magellanschen Wolke zu untersuchen, nach Durchführung einer Himmelsuntergrundsubtraktion zur Bereinigung der Spektren, gefolgt von einer Vollspektrumanpassung unter Verwendung der penalized pixel fitting Routine. Ich habe eine mittlere Radialgeschwindigkeit von 273 ± 1 km s^{-1} und eine Geschwindigkeitsdispersion von $\sigma_V = 31 \pm 1$ km s^{-1} abgeleitet. Die räumliche Verteilung der Geschwindigkeiten ist konsistent mit der bekannten Rotation der LMC-Scheibe, wobei Sterne auf der sich entfernenden Seite der Galaxie höhere Geschwindigkeiten aufweisen. Um zu untersuchen, wie Radialgeschwindigkeiten zwischen Sternpopulationen unterschiedlichen Alters variieren können, wird das Farb–Helligkeits-Diagramm in Regionen unterteilt, die Sternen in unterschiedlichen Entwicklungsstadien entsprechen. Eine Region, die junge (~ 20 Myr) Hauptreihensterne umfasst, hat eine mittlere Geschwindigkeit von 291 km s^{-1} und hebt sich deutlich gegenüber dem Bereich 265–285 km s^{-1} der anderen Regionen ab. Die Mehrheit ihrer Sterne mit hoher Geschwindigkeit befindet sich in der bekannten Sternentstehungsregion Shapley Constellation III. Es ist plausibel, dass diese Sterne aus einer dynamisch beschleunigten Gaswolke entstanden sind und deren Geschwindigkeit geerbt haben. Die zweitjüngste Region, die Hauptreihensterne leicht höheren Alters beherbergt, zeigt die niedrigste mittlere Radialgeschwindigkeit in der Stichprobe und weist eine geringe räumliche Überlappung mit Shapley Constellation III auf. Einige Sterne in diesem Gebiet zeigen niedrige Geschwindigkeiten, was möglicherweise darauf hinweist, dass sie vor dem Ereignis entstanden sind, das das Gas beschleunigte. Schließlich vergleiche ich die Kinematik junger (< 1 Gyr) und alter (> 1 Gyr) Populationen und finde ähnliche mittlere Geschwindigkeiten (276 ± 1 vs 273 ± 1 km s^{-1}, jeweils) und Dispersionen (31 ± 1 km s^{-1} für beide).

Statement of Originality

I hereby declare that this thesis is the product of my own work. All the assistance received in preparing this thesis and all the sources used, to the best of my knowledge, have been acknowledged.

Contents

List of Figures

List of Tables

List of Acronyms

2MASS Two Micron All-Sky Survey

AGB Asymptotic giant branch

CMD Color-magnitude diagram

Dec Declination

DR Data Release

dSph Dwarf spheroidal galaxy

ESO European Southern Observatory

FLAMES Fiber Large Array Multi Element Spectrograph

HR High Resolution

IFU Integral Field Unit

ISM Interstellar medium

LMC Large Magellanic Cloud

LR Low Resolution

MCs Magellanic Clouds

MCMC Markov Chain Monte Carlo

MW Milky Way

NIR Near-infrared

OGLE Optical Gravitational Lensing Experiment

pPXF Penalized pixel fitting routine

PM Proper motion

RA Right ascension

RC Red clump

RGB Red giant branch

RV Radial velocity

SC III Shapley Constellation III

SDSS Sloan Digital Sky Survey

SFH Star formation history

SMC Small Magellanic Cloud

Sm Magellanic spirals

SNR Signal-to-noise ratio

TOPCAT Tool for OPerations on Catalogues And Tables

UVES Ultraviolet and Visual Echelle Spectrograph

VIDEO VISTA Deep Extragalactic Observations Survey

VIKING VISTA Kilo-Degree Infrared Galaxy Survey

VIRCAM VISTA InfraRed CAMera

VISTA Visible and Infrared Survey Telescope for Astronomy

VHS VISTA Hemisphere Survey

VLT Very Large Telescope

VMC VISTA survey of the Magellanic Clouds system

VVV VISTA Variables in the Via Lactea

XSL X-Shooter Spectral Library

Chapter 1

Introduction

The Magellanic Clouds (referred to from now on as “Clouds”; MCs) are the closest interacting pair of dwarf irregular galaxies, and for that, they serve as unique laboratories for the study of galaxy formation, stellar evolution, and gravitational interactions in the Local Group. Visible from the southern hemisphere and appearing as faint ”clouds” in the sky (Fig. 1.1), they consist of two galaxies, the Large Magellanic Cloud (referred to from now on as “Large Cloud”; LMC) and the Small Magellanic Cloud (referred to from now on as “Small Cloud”; SMC).
The Clouds are linked to each other and to the Milky Way (MW) by extended streams of stars and gas, showing that they are not isolated systems but rather part of a complex dynamical interaction that seems to continue to shape their evolution. Their proximity to the MW and active star-forming regions allows us to resolve individual stars in great detail, making the Clouds a well-resolved example and a valuable analog for more distant, unresolved systems.

The Small Cloud (bottom left in Fig. 1.1) is the less massive of the two galaxies, with a dynamical mass, derived from the rotation curve, of $\sim 2 \times 10^9\, M_\odot$ (Stanimirović et al., 2004) and a stellar mass of $\sim 5 \times 10^8\, M_\odot$ (Rubele et al., 2018). It has a lower abundance of heavy elements compared to the Large Cloud, indicating a more primitive chemical composition (e.g. Russell & Dopita, 1992). The SMC center has a distance to the MW of $\sim$ 62 kpc, with a line-of-sight depth (distance difference between the nearest and most distant system) of $\sim$ 10 kpc (Muraveva et al., 2018; Graczyk et al., 2020). Despite its small size, the SMC exhibits active star formation in several regions (e.g. Livanou et al., 2007), offering valuable insights into stellar populations in low-metallicity environments.

The Large Cloud (top right in Fig. 1.1) is more massive and luminous, with a barred disk structure, making it the most prominent satellite of the MW. Located at a declination of about $-69°$, it extends over more than 7° in the southern celestial hemisphere. Measuring the distance to the LMC is of great importance, since it plays a key role in cosmology and in the determination of the Hubble constant. For this reason, the LMC distance has been the subject of numerous studies over the years and has been measured using a variety of independent meth-

Figure 1.1: Photo of the Large (top right) and the Small (bottom left) Cloud, a pair of gravitationally interacting dwarf irregular galaxies in the Local Group, visible from the southern hemisphere. Taken on 3 December 2009. Credit to: ESO/S. Brunier.

ods. The currently most accepted estimate places the LMC at a distance of 49.59 kpc, obtained from 20 binary systems, with an uncertainty of approximately 1% (Pietrzyński et al., 2019). Its northeastern regions are slightly closer to the MW than the southwestern parts, reflecting a tilt relative to our galaxy. With a total mass of around 1.8 x 10^{11} $M_{\odot}$, estimated from the kinematics of 30 globular clusters (Watkins et al., 2024), the LMC is the fourth largest galaxy in the Local Group, after Andromeda, the Milky Way, and the Triangulum Galaxy.

This Master's project aims to analyze the kinematics of stars in different regions of the LMC, based on El Youssoufi et al. (2023), who performed a similar analysis in the SMC. The research focuses on retrieving the radial velocities (velocity component on the line-of-sight; see section 1.4) of a sample of around 4000 spectra extracted from the European Southern Observatory (ESO) archive and selected using data from Gaia and near-infrared (NIR) photometry from the Visible and Infrared Survey Telescope for Astronomy (VISTA) survey of the Magellanic Clouds system (VMC) and the VISTA Hemisphere Survey (VHS). The velocities are then derived by performing a full spectrum fitting routine (pPXF).

Before diving into the methods and analysis, this first chapter outlines the history of the Clouds' discovery and the controversy that their name carries. It then provides an in-depth description of the Large Cloud, with a detailed description of its structural properties and morphological characteristics. A description of the observational instruments and datasets used in this project will follow. Finally, the chapter introduces the basic concepts of stellar motion and briefly presents the scientific motivation behind this work.

1.1 History of the discovery of the two Clouds and controversy of their name

The Magellanic Clouds are named after Fernão de Magalhães (Ferdinand Magellan in English), best-known for being the first European to open a maritime trade route to Asia across the Pacific Ocean in 1519.

However, Magellan was not an astronomer and was not the first to describe the two Clouds: the Small and the Large Clouds were known in the southern hemisphere since prehistoric times, long before Europeans; petroglyphs and rock drawings in Chile are the earliest preserved illustrations of them. Even if these populations had no written language, some oral knowledge has persisted: according to Dennefeld (2020), the Tupi-Guarani people from the Rio de Janeiro region in Brazil interpreted the two Clouds as fountains, with a tapir (associated with the LMC) or a pig (associated with the SMC) drinking from them. In the same water-themed context, the Mapuche people of Chile described them as ponds, known in their language as Rüganko or Menoko, located in the Wenu Mapu, the upper world or heavens, and linked to the Wenu Leufu, the "river above" corresponding to the Milky Way. This association suggests that the relationship between the MW and the MCs was already conceptually recognized a long time ago. A more spiritual and religious interpretation is found among the Kamilaroi of present-day Australia, who regard the Clouds as the place where souls go after death, and the Arimi of modern-day Tanzania, who envision them as a man and a woman assisting the Pleiades in bringing heavy rains during the rainy season (de los Reyes, 2023).

The earliest known record of sky observations that might reference the Clouds seems to be the Suwar al-Kawakib (Book of Fixed Stars), written around 964 by the Persian astronomer Abd-al-Rahman al-Sufi. In his book *"Historische Untersuchungen über die astronomischen Beobachtungen der Alten"* ("Historical investigations on the astronomical observations of the ancients"; Ideler, 1806), chronologist and astronomer Ludwig Ideler, translating it into German, includes the following statement:

> *"Unter den Füssen des Suhel (the classical name for Canopus) steht, wie einige behaupten, ein weisser Fleck, … den man in Tehama El-bakar, den Ochsen nennt."*
>
> *"Under the feet of the Suhel (the classical name for Canopus) stands, as some claim, a white spot, …which is called in Tehama El-bakar, the Ox."*

Even if no coordinates were given, it is believed that this refers to the Large Cloud, which, under favourable weather conditions, could be seen from southern Arabia. Around 1516, Italian explorer Andrea Corsali travelled to Cochin on the southwest coast of India. He wrote two letters (Corsali, 1516) describing his experiences and the southern sky, containing also a drawing clearly showing the two Clouds (Fig. 1.2). In one, dated January 6th, 1515, he wrote:

> *"Il polo antartico non ha stella alcuna della sorte del polo artico, ma si veggon molte stelle congregate insieme, che sono come due nebule [the Clouds], un poco separate l'una dall'altra, e un poco oscure nel mezzo. Tra queste ne sono due, non molto grandi né molto lucenti, che poco si muovono: e quelle due sono il Polo antartico."*

> *"The Antarctic pole has no star of the same nature as the Arctic pole, but many stars can be seen gathered together, forming something like two nebulae [the Clouds], slightly separated from each other and somewhat dark in the middle. Among them, there are two stars, not very large nor very bright, that move little: and those two are the Antarctic pole."*

From the early 19th century, with the increase of detailed observations, interest in the Clouds also grew. In 1828, James Dunlop made the first precise sketches of the MCs, while John Herschel cataloged numerous star clusters and nebulae within them, providing a systematic foundation for future studies. In the early 20th century, Henrietta Swan Leavitt discovered the period-luminosity relation of Cepheids in the MCs. Thanks to these measurements, it was finally understood that the Small and Large Clouds are two galaxies separated from the Milky Way, laying the groundwork for the modern understanding of the scale of the Universe.

It was in a scientific publication in 1847 that William Herschel used for the first time the name "Magellanic Clouds", in a section entitled *"On the two nubeculae or Magellanic Clouds"* (Herschel, 1847), suggesting that both terms were still in use at the time. It seems that by the late 19th century, the term Nubecula was still being used in scientific settings, but the term "Magellanic Clouds" was starting to move from nautical circles to the public and scientific spheres, replacing Nubeculae Major and Minor only once scientists officially abandoned Latin (Dennefeld, 2020).

The problem with the choice of dedicating the Clouds to him is not just that Magellan was not the one who discovered the two Clouds, nor was he an astronomer. During his voyage around the globe, he enslaved, killed, and burned down the home of Indigenous people. Unfortunately, despite his controversial actions, Magellan's name is one of the most recognizable in astronomy. The upcoming Giant Magellan Telescope[1], currently under construction at Las Campanas Observatory in Chile's Atacama Desert and expected to be completed in 2029, is only the latest example of how his name continues to be celebrated in astronomy. With over

---

[1] `https://giantmagellan.org/`

Figure 1.2: Italian explorer Andrea Corsali's drawing of the Southern Cross and the Clouds in a letter to Giuliano de Medici, 1516. Credit: State Library of New South Wales.

17,000 peer-reviewed articles bearing his name, alongside a lunar crater, a Martian crater, and the NASA Magellan spacecraft (de los Reyes, 2023), his presence in the field is hard to ignore. The fact that these telescopes named after him are located in Chile, a country with a history shaped by the violent Spanish conquest, is almost poignant: it was Magellan's "discovery" of the Strait that bears his name that allowed Spanish conquistadors to explore Chile's coastline, which eventually led to genocidal campaigns against the native Mapuche people.

Because of all of these reasons, in her article in the journal APS Physics, astronomer Mia de lo Reyes calls for the International Astronomical Union to rename the Magellanic Clouds and the other astronomical institutions: "I and many other astronomers believe that astronomical objects and facilities should not be named after Magellan, or after anyone else with a violent colonialist legacy. [...] Names reflect community values. Naming objects, buildings, and places after people has long been a way for society to honor individuals for their discoveries, their accomplishments, or the values they symbolize. Magellan made no astronomical discoveries, and for many, he continues to be a symbol of imperialist and anti-Indigenous violence. [...] When we uphold the names of people, such as Magellan, whose lives and legacies have actively caused harm, we alienate the communities who have been harmed. The communities that suffered because of Magellan have rich astronomical traditions that are often less valued than Western ones. Even within the field of professional astronomy, the repercussions of Spanish colonization continue to this day. For example, I am the first woman of primarily Filipino descent to become an astronomy professor in the United States, in part because lack of access to resources has historically prevented Filipinos from participating in astronomy research." (de los Reyes, 2023; page 2).

1.2 The Large Cloud

The Large Cloud (Fig. 1.3), at a distance of approximately 50 kpc (Pietrzyński et al., 2019), is one of our closest neighbours and, as a result, stands as the most studied example of an irregular galaxy. Being one of the most easily observable galaxies from our vantage point in the MW, it has become a benchmark for studies on various topics. It is a key target for research on stellar populations and the interstellar medium (ISM), is being used to study the presence of dark objects in the Galactic Halo through microlensing, and, as already mentioned, it plays a fundamental role in determinations of the cosmological distance scale. For these reasons, having an understanding of the structure and kinematics of the LMC is essential (van der Marel, 2006).

The LMC is a gas-rich galaxy, and its stars are distributed irregularly and asymmetrically in a flat disc tilted at an inclination of $i \sim 30°$ with respect to the line-of-sight (e.g Ripepi et al., 2022; Gaia Collaboration et al., 2021), even though there remains a large uncertainty in the literature on what the inclination angle is. The galaxy exhibits an asymmetric morphology, with an offset bar and a dominant spiral arm shaping its appearance, characteristics that define a whole family of galaxies known as Magellanic spirals (Sm; Ruiz-Lara et al., 2020). These galaxies are quite common in the Universe and are among the most structurally lopsided systems observed (de Vaucouleurs & Freeman, 1972). The origin of their asymmetry still remains unknown, especially concerning the formation of their signature spiral arm. Within the different sub-categories of Sm galaxies, the LMC is classified as an SBm system, i.e. a Magellanic barred spiral galaxy.
There have been many investigations focused on the LMC and its different stellar populations. These studies have revealed various morphological properties of the galaxy depending on the age of the stars: for example, Cioni et al. (2000) showed that older stars (with ages > 0.5 Gyr), dominate the galaxy's mass and tend to form a regularly distributed structure, while younger populations (age < 0.5 Gyr) display more irregular arrangements with spiral arms and tidal features.

The asymmetrical bar, one of the most striking features of LMC, is prominent and visible in optical and NIR wavelengths but absent in the HI gas distribution (Subramaniam & Subramanian, 2009). It is offset from the center of the outer disk by ~ 1 kiloparsec (e.g. de Vaucouleurs & Freeman, 1972; Rathore et al., 2025b) and appears to be elliptical in the south-east and flat in the north-west. The bar is also warped so that the east and west ends are closer to the MW than the middle (e.g. Subramaniam, 2003). Recent N-body hydrodynamical simulations suggest that a collision between the LMC and SMC about 150 Myr ago can explain the

Figure 1.3: Color composite image of the LMC, where the Y band is shown in blue, J in green, and K_S in red. Credit: ESO/VMC Survey (Cioni et al., 2011).

unusual properties of the LMC's bar (Rathore et al., 2025a). In their analysis, they show that before the collision, the simulated bar was centered, co-planar, and had a gaseous counterpart. After the collision, the simulated bar is displaced by ~ 1.5 kpc, inclined by $\sim 8.6°$, and gas-free, indicating that the interaction with the SMC had a significant impact on the structure of the LMC's bar.

The observed asymmetries in the LMC have often been attributed to tidal interactions and minor mergers. Besla et al. (2012), studied the specific case of the LMC-SMC-MW system, using N-body smoothed-particle hydrodynamics simulations to model the interactions between the three galaxies. They found that such interactions can explain the LMC's off-centered bar and single arm, as well as the observed large-scale features (see next paragraph). Their work suggests that the main drivers of the observed morphology and configuration of the LMC are most likely interactions between the LMC and the SMC, while the MW had only a minor influence. The rarity of triple systems like LMC-SMC-MW, compared to the widespread presence of S(B)ms in the Universe, supports this interpretation, suggesting that asymmetric spiral structures can develop even without a nearby MW-like galaxy (Ruiz-Lara et al., 2020).

Magellanic System

The close encounters between the two Clouds created two structures connecting the Large and Small Clouds: the Magellanic Bridge and the Magellanic Stream, shown in Figure 1.4.

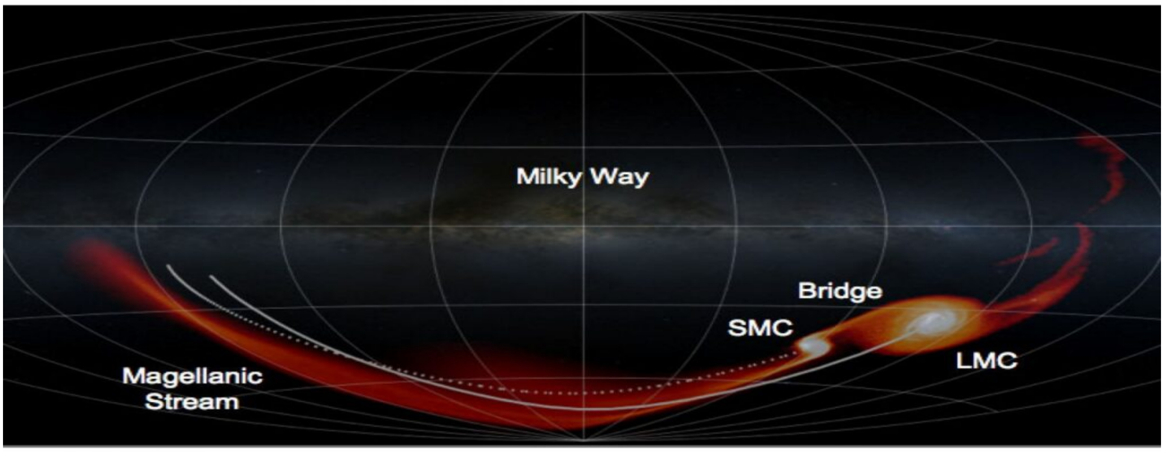

Figure 1.4: Simulated gas distribution of the Magellanic System. The entire sky is plotted in galactocentric coordinates of longitude and latitude. The continuous line shows the calculated path of the LMC, while the dotted line is that of the SMC. The color range from dark to light indicates the density (from lower to higher) of the hydrogen gas comprising the Magellanic Stream and the Bridge connecting the two dwarf galaxies. Credit: Besla et al. (2010); MW background image by Axel Mellinger.

The Bridge, discovered by Hindman et al. (1963), is a continuous stream of mostly neutral hydrogen gas that connects the two Clouds, traveling from the SMC to the LMC, but it also exhibits a stellar population with a mass of 1.5 x 10^4 $M_\odot$ (Harris, 2007); early observations revealed young stars, particularly in its western part with notable density clumps, but more recent studies have identified intermediate-age and old stars (∼400 Myr to 5 Gyr) as well (e.g. Bagheri et al., 2013). Skowron et al. (2014) detected a young stellar population even in the eastern part (even though the number densities in that region are much lower than in the western Bridge), proving that there is a continuous stream of young stars that connects the MCs. They also found that the intermediate-age population, such as red giant branch (RGB), asymptotic giant branch (AGB) and red clump (RC) stars extends symmetrically into the Bridge with clear inter-Cloud continuity (suggesting tidal stripping), whereas the old population (bottom RGB) exhibits only minor LMC/SMC mixing in the southern Bridge, consistent with slight halo overlap.

The Stream, first sighted in 1965 (Dieter, 1965) and linked to the Clouds in 1974 (Mathewson et al., 1974), is an extended tail of neutral and ionized gas trailing the Clouds in their orbit around the Milky Way. Mathewson et al. (1974) also detected a counterpart to the Stream on the other side of the Clouds, the Leading Arm. When considered with its Arm, the Stream stretches over 200° across the sky (D'Onghia & Fox, 2016), making it one of the most prominent gaseous structures in the vicinity of the MW. The total mass of the Stream is ∼ 2 x 10^9 $M_\odot$, consisting of HI (∼ 4 x 10^8 $M_\odot$; Brüns et al., 2005) and ionized gas (∼ 1.5 x 10^9 $M_\odot$; e.g. Barger et al., 2017).

1.2.1 Outskirts of the LMC

The stellar outskirts of the Clouds show a complex morphology characterized by several substructures and stellar overdensities. These features are illustrated in Fig. 1.5, which shows maps of the stellar periphery derived from NIR data from the VHS (El Youssoufi et al., 2021).

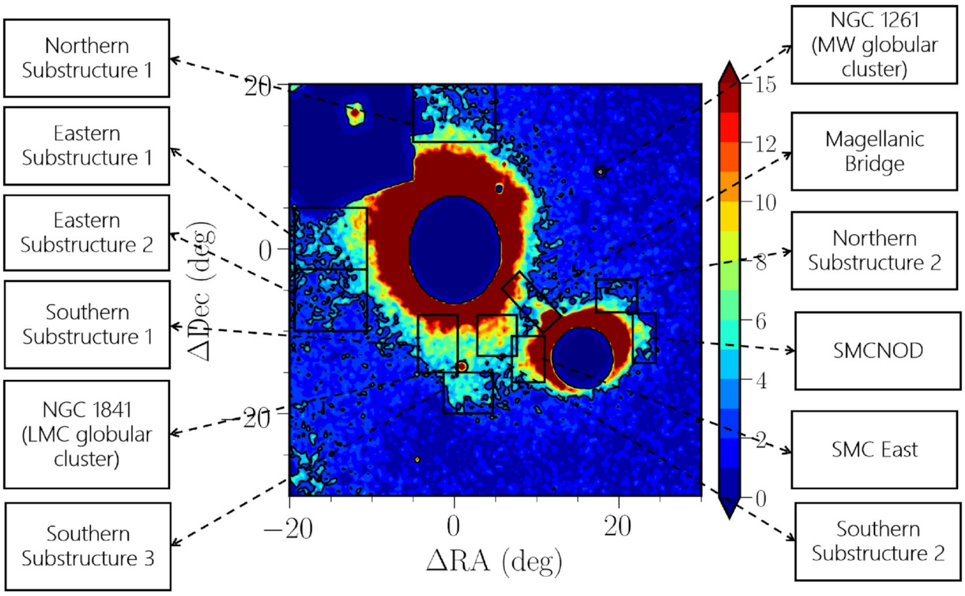

Figure 1.5: Stellar substructures of the Clouds as revealed by El Youssoufi et al. (2021). Prominent features in the outskirts of the LMC include Northern Substructure 1, Eastern Substructures 1 and 2, and Southern Substructures 1–3. Coordinates are given as offsets in RA and Dec relative to the LMC center at $(\mathrm{RA}_0, \mathrm{Dec}_0) = (81.24°, -69.73°$; de Vaucouleurs & Freeman, 1972).

One of the most prominent features is the Northern Substructure 1, located at Right Ascension (RA) = 81.24°, Declination (Dec) = −54.73° (van der Marel & Cioni, 2001). This structure is particularly prominent in the old stellar population (RGB, AGB and RC stars) and extends up to $\sim 20°$ from the LMC optical center (RA = 81.24°, Dec = −69.73°), although it is also present among younger stellar populations.

On the eastern side of the LMC, two additional substructures have been identified at approximately (RA = 66.24°, Dec = −68.73°) and (RA = 66.24°, Dec = −75.73°), both oriented toward the Galactic disc. Within the young stellar population, traced by the tip of the main sequence and supergiant star, Eastern Substructure 1 (first reported by de Vaucouleurs, 1955) forms an approximately circular feature, while Eastern Substructure 2 (El Youssoufi et al., 2021) appears as a thin stellar stream.

South of the LMC, Southern Substructure 1 (RA = 79.24°, Dec = −82.23°) and Southern Substructure 2 (RA = 87.24°, Dec = −79.73°) are found (Mackey et al., 2018), both of which are more evident in the old stellar population (El Youssoufi et al., 2021). Even further south, a low-density stellar extension surrounds the globular cluster NGC 1841, forming Southern Substructure 3 at approximately (RA = 83.24°, Dec = −87.23°). However, its physical connection with Southern Substructure 1 remains uncertain. While Southern Substructures 1 and 3 are particularly evident in maps based on LMC proper motions, Southern Substructure 2 also appears in maps derived from the Small Magellanic Cloud, suggesting a possible dynamical link between the two systems.

1.3 Observational Data and Instruments

For this project, I worked with spectra collected from the fiber Large Array Multi Element Spectrograph (FLAMES) and photometric data from the VISTA surveys. The following section gives a short description of the instruments and datasets used.

1.3.1 Photometry: the VISTA Surveys

Photometry deals with measuring the brightness of stars through different filters, providing information about their luminosity and colors. This technique is useful for selecting stellar samples, allowing us to distinguish between different stellar populations and to construct color–magnitude diagrams (CMDs), used to identify stars' evolutionary stages and to determine their properties.

The photometric data used in this study come from VISTA (Sutherland et al., 2015), a 4.1-meter specialized wide field survey telescope for the southern hemisphere, located at the Paranal Observatory in northern Chile, on the peak adjacent to the one hosting the ESO Very Large Telescope (VLT), sharing the same exceptional observing conditions. The telescope was specifically designed to conduct large-scale imaging surveys of the sky at NIR wavelengths.
At the heart of the telescope there is VIRCAM (VISTA InfraRed CAMera), a powerful wide-field NIR camera with 16 infrared-sensitive detectors arranged in a mosaic. This configuration provides a total field of view of about 1.65 deg^2 per pointing, making VISTA extremely efficient at covering large sky areas in a relatively short amount of time. Observations are carried out through five broadband filters, Z (0.90 μm), Y (1.02 μm), J (1.25 μm), H (1.65 μm), and K_S (2.15 μm), and three narrow band filters at 0.98, 0.99, and 1.18 μm.

There are six large public surveys being carried out by VISTA (VISTA Surveys), as shown in Fig. 1.6: UltraVISTA, VISTA Kilo-Degree Infrared Galaxy Survey (VIKING), VISTA Magellanic Survey (VMC), VISTA Variables in the Via Lactea (VVV), VISTA Hemisphere Survey (VHS), VISTA Deep Extragalactic Observations Survey (VIDEO). They cover different areas of the sky to different depths to try to answer a wide range of scientific questions.

Within these several surveys, two are relevant for this work: the VMC and the VHS (Fig. 1.7). Both provide NIR photometry, but with different scientific goals, observational strategies, and sky coverage, making them complementary datasets for the study of the MCs and their stellar populations.

The VMC survey (Cioni et al., 2011) led by Principal Investigator Maria-Rosa Cioni is a deep, homogeneous, and uniform survey specifically designed to cover the entire Magellanic System, including the LMC, the SMC, and the Bridge. Its main scientific goals are the determination of the spatially resolved star formation history (SFH) and the three-dimensional geometry of the Magellanic system. VMC achieves this by obtaining multi-epoch photometry in the Y, J, and K_S bands, reaching sources 6 mag fainter compared to other surveys, which sample down to only upper red giant branch stars. VMC data cover the full RGB population, short-period variable stars, and reach down to the oldest main sequence turn-off stars.

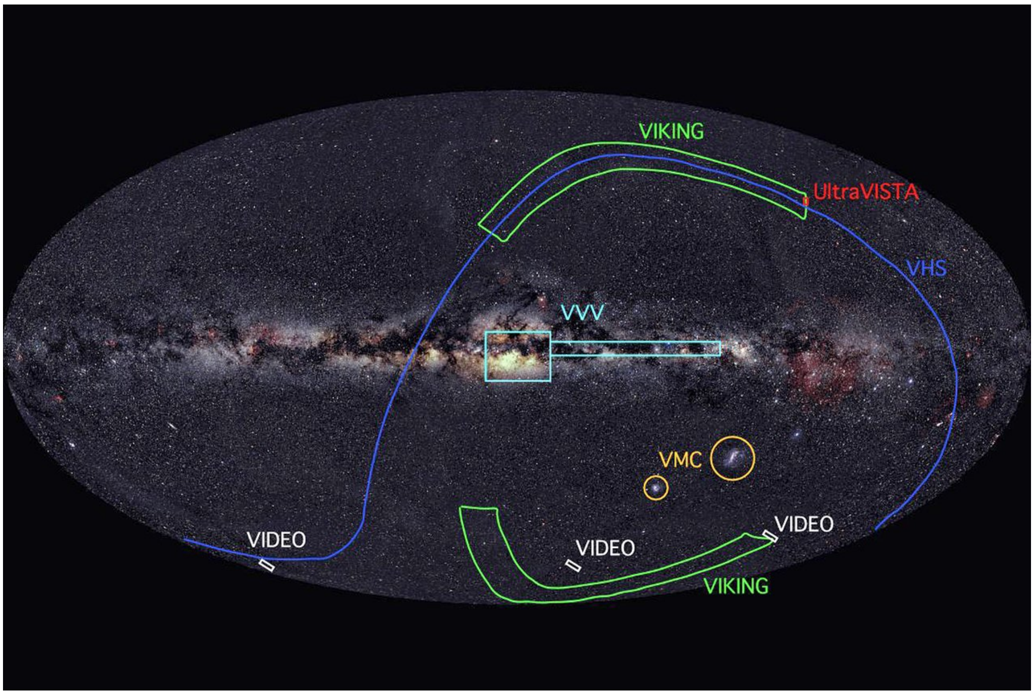

Figure 1.6: Representation of the sky coverage of the six VISTA surveys: UltraVISTA, VISTA Kilo-Degree Infrared Galaxy Survey (VIKING), VISTA Magellanic Survey (VMC), VISTA Variables in the Via Lactea (VVV), VISTA Hemisphere Survey (VHS), VISTA Deep Extragalactic Observations Survey (VIDEO). Credit: VISTA/ESO.

The VHS survey (McMahon et al., 2013) led by Principal Investigator Richard G. McMahon, on the other hand, is a wide-area, multi-band, NIR survey that, when combined with other VISTA public surveys (i.e., VIKING, VVV, and VMC surveys), results in the coverage of the whole southern celestial hemisphere. The main aims of VHS are to examine low-mass and nearby stars, to study the merger history of the MW, to measure the properties of dark energy through the examination of large-scale structure, and to search for high-redshift quasars.

VHS includes three programs (see Fig. 1.7): (1) VHS-GPS (Galactic Plane Survey), which covers a region of ~ 8200 deg^2 with J and K_S filters; (2) VHS-DAS (Dark Energy Survey), which observed ~ 4500 deg^2 with J, H, and K_S filters; and (3) VHS-ATLAS, which observed ~ 5000 deg^2 evenly divided between North and South Galactic caps with Y, J, H, and K_S filters.

By combining VMC and VHS, we benefit from both depth and wide coverage: VMC offers detailed insight into the faint stellar populations, while VHS ensures uniform photometry across a much larger spatial extent.

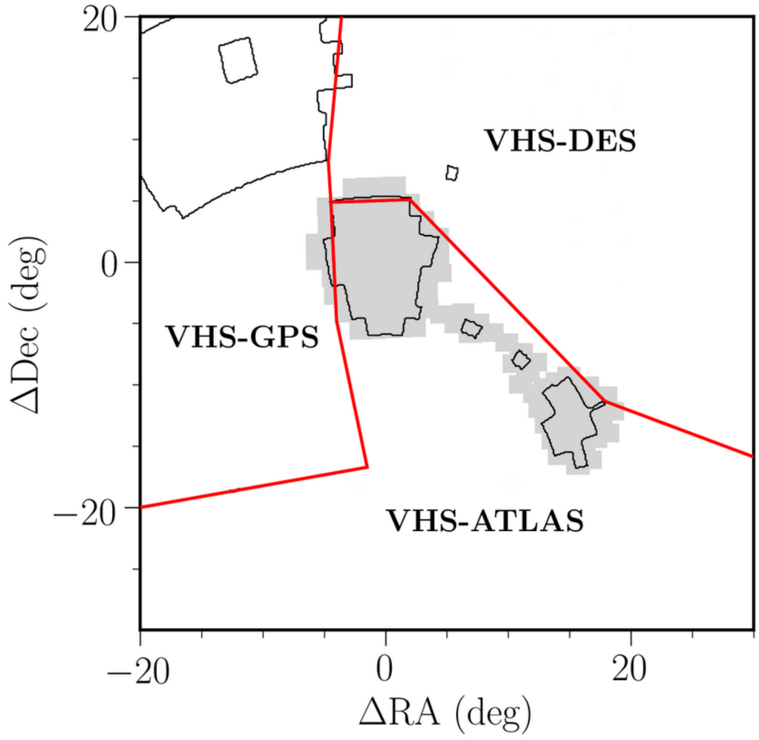

Figure 1.7: Representation of the main photometric surveys used in this work: VHS and VMC. The projection origin of the maps is set at $(\mathrm{RA}_0, \mathrm{Dec}_0) = (81.24°, -69.73°)$. The boundaries of the VHS sub-surveys are shown in red, while observational gaps are marked in black. The region covered by the VMC tiles is highlighted in light grey (El Youssoufi et al., 2021).

1.3.2 Spectroscopy: FLAMES

Spectroscopy is a powerful technique that allows us to split electromagnetic radiation into its constituent wavelengths and study celestial objects in detail: from the analysis of the spectrum of a star, we can derive information on its chemical composition, temperature, radial velocity, and distance. The spectra used in this study were obtained with the FLAMES instrument (Pasquini et al., 2002) and its main spectrograph GIRAFFE.

FLAMES is a multiobject, intermediate- and high-resolution spectrograph with 130 optical

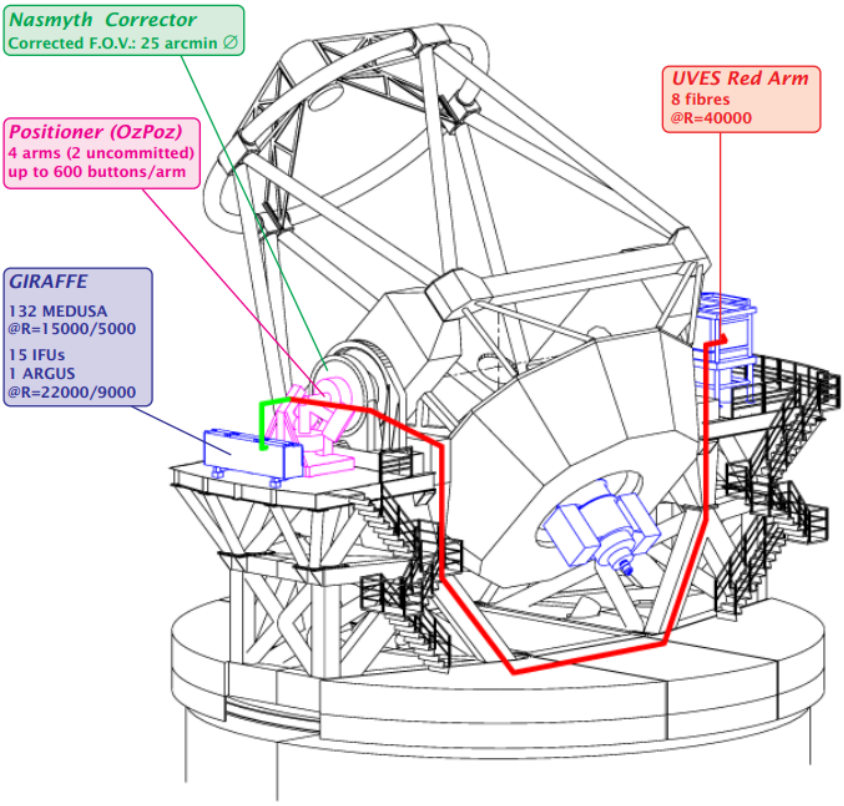

Figure 1.8: Schematic view of the fiber facility FLAMES at the VLT with its components: the optical corrector, the fiber positioner, and the two spectrographs GIRAFFE and UVES (Pasquini et al., 2000).

fibers, installed on the second Unit Telescope at the VLT. It covers a wide field of view (25 arcmin diameter) and consists of several components, illustrated in Fig. 1.8: an optical corrector, which provides excellent image quality over the full field of view; a fiber positioner (OzPoz), which helps with limiting the time between observations to less than 15 minutes; a link to the Ultraviolet and Visual Echelle Spectrograph (UVES) via eight single object fibers per plate; and the spectrograph GIRAFFE, with its own fibersystems (Pasquini et al., 2000).
Additionally, the observing software FLAMES OS controls the instrument subsystems and enables simultaneous UVES and GIRAFFE observations.

GIRAFFE, named after its original vertical design, is a medium- to high-resolution spectrograph (R $\sim$ 5,500–65,100) operating over the entire visible range (370–950 nm), from which the spectra used in this work were obtained. It was developed by the Observatoire de Paris-Meudon (P.I. F. Hammer) and the Observatoire de Genève (P.I. A. Blecha), in collaboration with ESO. It is equipped with high (HR) and low (LR) resolution echelle gratings and several filters to select the required spectral range.
The instrument is designed for high spatial density spectroscopy of galactic and extragalactic targets and is fed by a fiber system that allows simultaneous observations of multiple objects

across the field of view. The fiber system connected to GIRAFFE includes MEDUSA fibers, which allow up to 131 targets to be observed at the same time, several Integral Field Units (IFUs) composed of microlens arrays, and the ARGUS IFU, a larger integral field unit providing spatially resolved spectroscopy.

1.4 Stellar motion: radial velocity and proper motion

The motion of a star can be described as the combination of two components: the tangential motion, lying in the plane of the sky, and the radial motion, directed along the observer's line of sight (1.9). Together, these quantities provide the basis for reconstructing the three-dimensional kinematics of stellar systems.

The tangential component is usually expressed as proper motion (μ; PM), i.e., the apparent angular motion of a star across the sky with respect to more distant sources, measured in arcseconds per year. Once the distance d to the star is determined through astrometric means (e.g., parallax), μ can be converted into a physical tangential velocity, v_t, via the relation:

$$v_t = 4.74\, \mu\, d \tag{1.1}$$

where v_t is expressed in $\mathrm{km\,s^{-1}}$ if μ is given in $\mathrm{arcsec\,yr^{-1}}$ and the distance d in parsecs. The constant 4.74 comes from unit conversion.

Modern astrometric surveys, such as Gaia or the Sloan Digital Sky Survey (SDSS), provide both proper motions and parallaxes with high accuracy, making it possible to determine tangential velocities for millions of stars.

The radial velocity (v_r; RV) measures the motion of the star towards or away from the observer, thus it cannot be obtained through astrometry. Instead, it is retrieved from spectroscopy, by analyzing the Doppler shift of stellar absorption or emission lines.

For a single spectral feature with rest-frame wavelength λ_{rest}, the radial velocity is given by:

$$\frac{v_r}{c} = \frac{\Delta\lambda}{\lambda_{\text{rest}}} = \frac{\lambda_{\text{obs}} - \lambda_{\text{rest}}}{\lambda_{\text{rest}}}, \tag{1.2}$$

where λ_{obs} is the observed wavelength and c is the speed of light. A positive v_r corresponds to a redshift, meaning that the star is receding, while a negative v_r indicates a blueshift (the star is approaching).

To be more precise, even if the RV is commonly defined as the component of a star's motion along the observer's line of sight, when aiming at accuracies better than 1 $\mathrm{km\,s^{-1}}$, this definition is far too simplistic. The quantity obtained from spectroscopy is related to the wavelength shift measured in the barycentric frame and does not always correspond exactly to the true geometric velocity along the line of sight (Lindegren & Dravins, 2003). This is because the measured wavelength shift is affected not only by the star's motion, but also by relativistic effects, the motion of the observer, and the adopted reference frame.

When both tangential and radial components are available, the full space velocity of a star can be reconstructed. Its magnitude is

$$v_{\text{space}} = \sqrt{v_r^2 + v_t^2}. \tag{1.3}$$

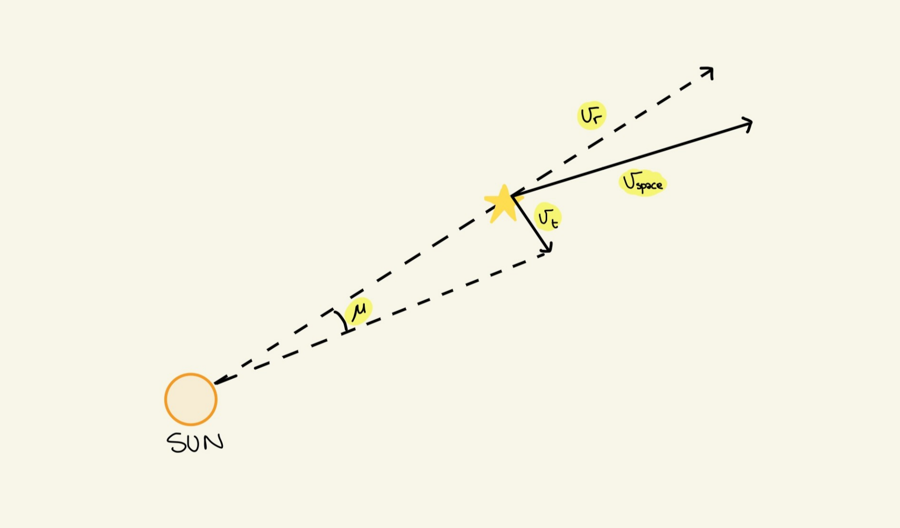

Figure 1.9: Diagram illustrating the relation between proper motion and the components of stellar velocity. The star's total space velocity (v_{space}) is the vector sum of the radial velocity (v_r) and the transverse velocity (v_t).

1.5 Scientific Motivation

As discussed in this introductory chapter, the unique characteristics of the Clouds offer a rare opportunity to study many aspects of astrophysics. Among these, their proximity to us makes it possible to resolve individual stars across a wide range of ages and masses, making them ideally suited for investigating stellar evolution, star formation, chemical enrichment, and the impact of galactic interactions on morphology.

In particular, stellar radial velocities trace the dynamical state of galactic disks, revealing rotation patterns and age-dependent kinematics, while anomalous velocities can reveal recent gravitational interactions. In the case of the LMC, its complicated morphology and interaction history with the SMC make it an especially interesting system for such an analysis.

This project aims to use these kinematic tracers to improve the current understanding of the structure and dynamical evolution of the LMC, and to investigate whether different stellar populations retain evidence of its interaction history.

Chapter 2

Sample Selection

Before carrying out the kinematic analysis, it was necessary to build a clean and reliable sample of stars belonging to the Large Cloud. The structure of this work and the selection of the stellar sample mirror those outlined in El Youssoufi et al. (2023), with some adjustments to better fit the characteristics of the LMC.
The procedure combines photometric and spectroscopic data from different surveys. These datasets were carefully cleaned by applying quality cuts and filtering out possible contaminants, such as foreground stars from the MW or sources with unreliable measurements. The visualization and cross-matching of the catalogs were performed using TOPCAT (Tool for OPerations on Catalogues And Tables; Taylor, 2011).

2.1 Photometry

To select a sample for our analysis, I started with NIR photometry from the VISTA survey already discussed in Section 1.3: the VMC and VHS. The VMC observed ~ 170 deg^2 until its completion in October 2018, covering 68 tiles across the LMC (105 deg^2), 27 across the SMC (42 deg^2), 13 across the Bridge (21 deg^2), and 2 within the Stream (3 deg^2). The data used for my study were part of the Data Release (DR) 6 (Cioni & et al., 2023), published in June 2023, which includes data from observations taken between November 2009 and October 2018, providing both newly released observations and updated versions of previously released data.
Regarding VHS, I used data from DR5 (McMahon et al. 2021), which includes image products of observations taken over 8 years, from November 2009 until 30th March 2017. The total sky coverage in at least one waveband is 16,730 square degrees, encompassing 1,374,207,485 sources.

From both VMC and VHS, aperture corrected magnitudes calculated within a 2 arcsec diameter in the J and K_s bands (`jAperMag3` and `K`$_S$`AperMag3`) were used, within 20 deg from the galaxy optical center (RA = 81.24°, Dec = −69.73°) at the epoch J2000. The initial selection criteria used are the following: objects that have at least a 70% probability of being stars (flag `mergedClass` = -1 or -2) and sources with minor quality issues (flag `K`$_S$`ppErrBits` ≤ 256 and `jppErrBits` ≤ 256). After applying these criteria, I obtained 3,835,896 and 2,612,607 stars from VMC and VHS, respectively. While combining the two samples, I took into account the overlap of VMC and VHS observations in the area of the Bridge by eliminating duplicate sources, keeping data from VMC. For the remaining stars, objects with photometric errors ≥ 0.1 in both bands were excluded. This resulted in a sample of 6,345,420 stars from the two VISTA Surveys.

For stars that are too bright for VMC and VHS, Two Micron All Sky Survey (2MASS; Skrutskie et al., 2006) photometry was used. The survey collected imaging data covering $\sim 99.9\%$ of the sky in the J, H, K_S bands. Observations were conducted from the dedicated 1.3 m diameter telescope located at Cerro Tololo, Chile, between June 1997 and February 2001.
From 2MASS, I required that stars were detected in both bands, with measurements made with a signal-to-noise ratio (SNR) > 10 and photometric errors < 0.1 (`flag ph qual` = AAA), measurements were made on six individual 1.3 s exposures covering the sources (`flag rd flg` = 222), one component was fit when estimating the brightness of the sources (`flag bd flg` = 111), and keeping only sources unaffected by known artefacts (`flag cc flg` = 000). Excluding common objects, 552,117 sources were added to the final sample.

A challenge that arises when studying stars in the LMC is the potential contamination from foreground stars belonging to the MW. To mitigate this issue and better isolate the stars in the LMC, we incorporated astrometric data from Gaia DR3 (Katz et al., 2023). To focus on stars belonging to the LMC and remove stars from the MW, we limited the sample to stars with a parallax value of $\omega < 0.2$, which helps filter out objects that are likely part of the MW. Additionally, we selected stars with proper motion values within the ranges $-2.5 < \mu_{RA} < 6.5$ and $-4 < \mu_{Dec} < 4$, ensuring that only stars with motions consistent with the LMC's motion were included in the analysis.

Lastly, variable stars were removed from our sample using the Optical Gravitational Lensing Experiment (OGLE) III and IV, a Polish astronomical project based at the University of Warsaw that has been running a long-term variability sky survey since 1992. The main targets of the experiment are the Clouds and the Galactic Bulge, and most of the observations have been made at the Las Campanas Observatory in Chile. From our sample, 135,783 variables were removed, including classic Cepheids, type II Cepheids, anomalous Cepheids, RR Lyrae stars, and long-period variables. These stars were excluded to avoid the influence of stellar pulsation velocity variations on the accuracy of our RV measurements.

The resulting photometric data set contains 3,170,027 sources, whose distribution in the CMD constructed using color J-K_S and the magnitude K_S is shown in Fig. 2.1. This catalog is extensively used throughout the analysis of the results presented in this work, mainly as a background reference to provide a global view of the stellar distribution within the galaxy.

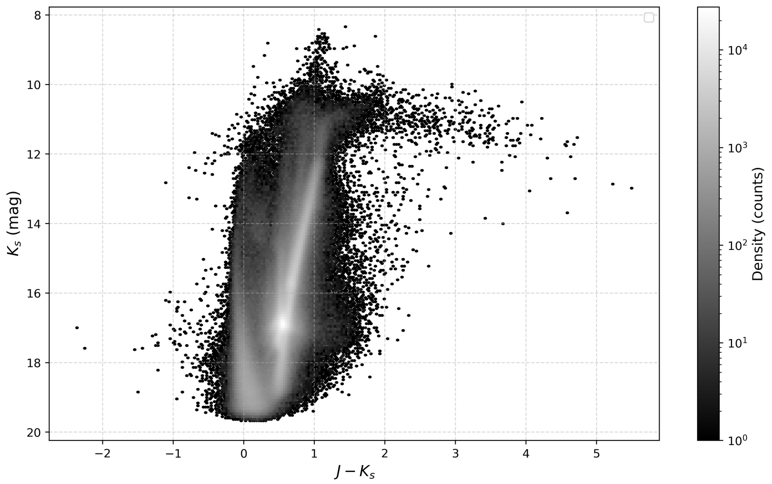

Figure 2.1: Density map of the full photometric sample in the J-K_S vs K_S CMD. The color bar shows the stellar density (number of sources per bin) on a logarithmic scale, with lighter colors corresponding to higher densities.

2.2 Spectroscopy

To find spectra that have photometric counterparts in our sample, I started by selecting all stars with 1D spectra within a 20-degree radius from the LMC optical center and with SNR $>$ 10 from the ESO Science Archive Facility (ESO SAF[1]). After applying these selection criteria, the cross-matching was carried out with a maximum separation of 1 arcsec, resulting in a sample of 4,801 objects.

Most of the objects had multiple observations, covering different wavelength ranges and with different resolutions (R) and SNR values. For each star, I selected only one spectrum, prioritizing the highest-resolution spectrum. In the event of a tie, I chose the spectrum with the higher SNR.

Figure 2.2 shows the distribution of key characteristics of our spectra, including observation date, resolving power R, instrument, and SNR. The spectroscopic sample spans observations collected between 2001 and 2024 (Fig. 2.2a), with clear concentrations in a few specific years corresponding to major observing campaigns. The resolving power distribution (Fig. 2.2b) of the spectroscopic sample is rather inhomogeneous, showing four main peaks, depending probably on the different setups, while the signal-to-noise ratio (Fig. 2.2d) decreases steeply, with most spectra having SNR between 10 and 50. As shown in Figure 2.2c, of these almost 5,000 spectra, approximately 95% (4,559 stars) were detected using the GIRAFFE spectrograph of FLAMES (Section 1.3.2). The analysis will focus only on these objects to avoid inaccurate systematic uncertainties.

---

[1] `https://archive.eso.org/scienceportal/home`

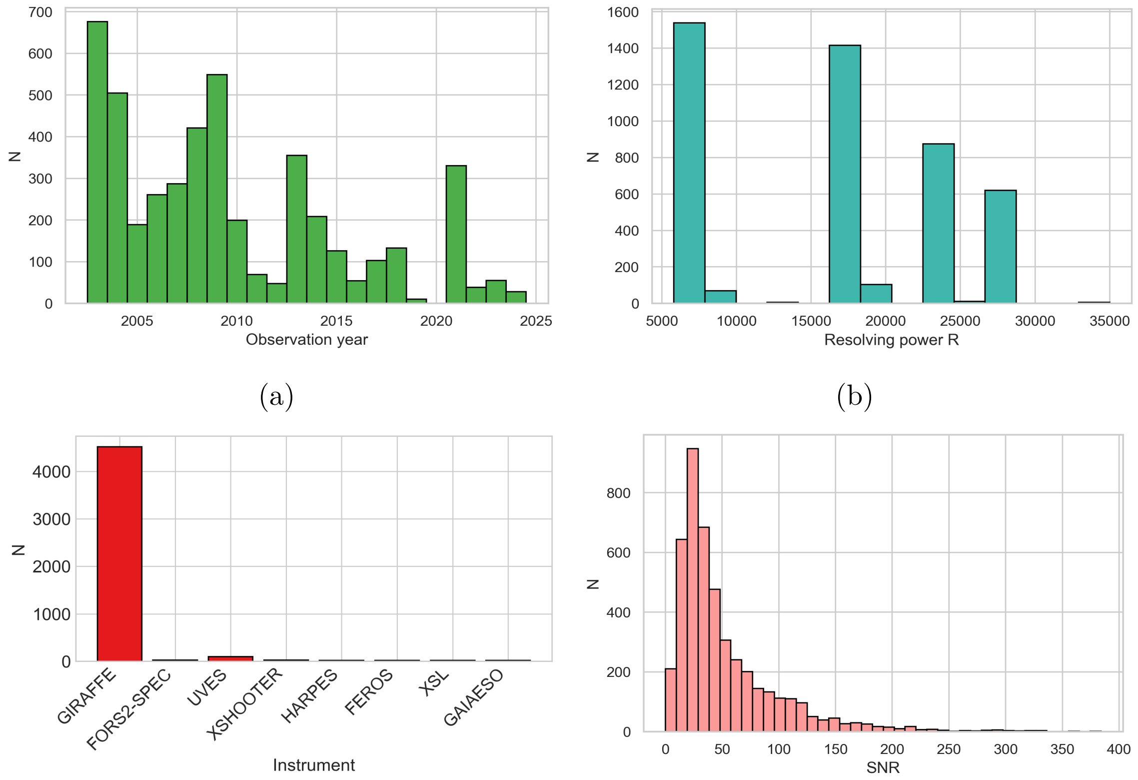

(a) (b)

(c) (d)

Figure 2.2: Histograms showing the distribution of the spectra in the sample as a function of observation date (a), resolving power R (b), instrument (c), and SNR (d). In all panels, the x-axis represents the corresponding parameter, while the y-axis shows the number of spectra.

Figure 2.3 shows the distribution in space (a) and the CMD (b) of the sample of this study. In both figures, the grey scale indicates the stellar density on a logarithmic scale and represents the sample obtained from the photometric data selection described in Chapter 2.1, while red points refer to stars with available spectra in the ESO archive.

In panel (a) of Fig. 2.3, the spatial distribution is shown deprojected onto the LMC tangent plane centered at $(\alpha_0, \delta_0) = (81.24°, -69.73°)$ using the zenithal equidistant projection. Coordinates are transformed from equatorial (α, δ) to Cartesian (X, Y) via the spherical trigonometry formulae (van der Marel & Cioni, 2001):

$$X \equiv \theta \cos \phi \tag{2.1}$$

$$Y \equiv \theta \sin \phi \tag{2.2}$$

where θ is the angular distance between each star (α, δ) and the LMC center (α_0, δ_0), computed via the spherical cosine rule, and ϕ is the position angle of the star measured counterclockwise from the local direction of decreasing right ascension (at constant δ_0) on the celestial sphere.

It is worth noting that the spectroscopic sample of 4559 stars represents only a small fraction of the full photometric catalog and may not be fully representative of the LMC's overall stellar population, as the spectra were collected from archival observations designed for different scientific programs. In particular, certain evolutionary stages or spatial regions of the galaxy might be over- or under-represented. For example, as visible in panel (a) of Fig. 2.3, the spectroscopic targets are predominantly concentrated in the northern regions of the galaxy, with the southern and outer parts of the disk remaining largely unsampled.

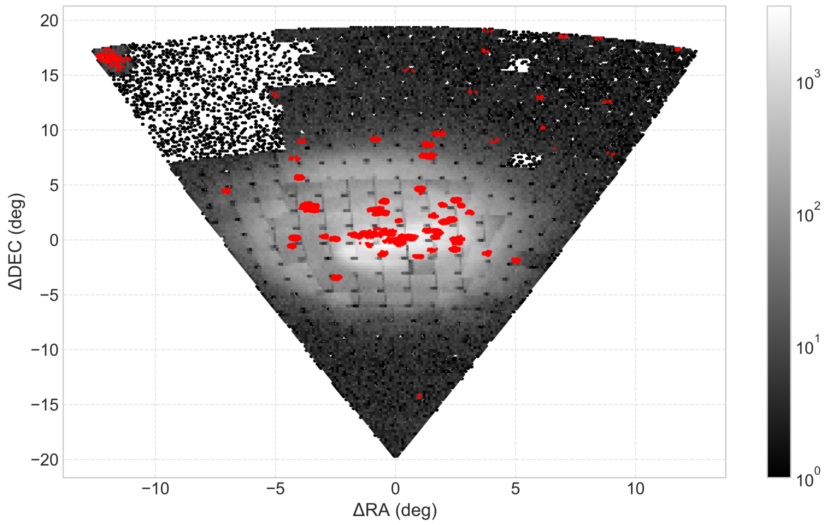

(a)

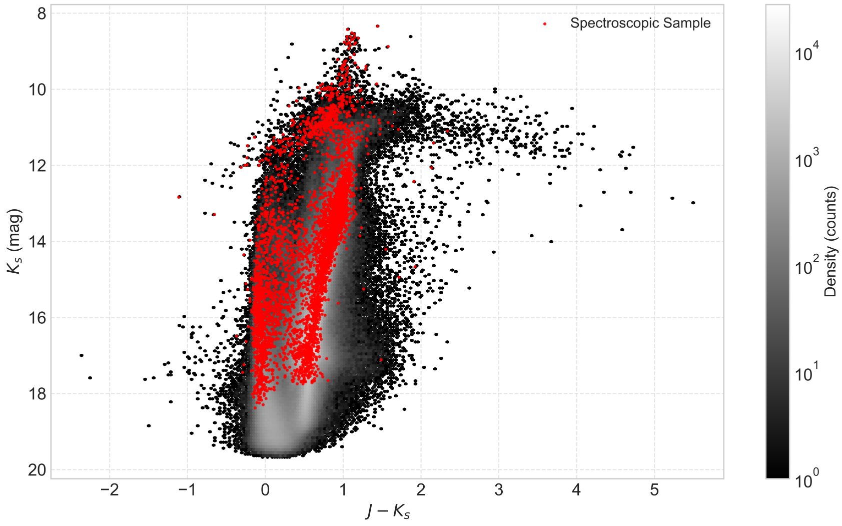

(b)

Figure 2.3: Top: spatial distribution of the photometric sample in the ΔRA–ΔDec plane (deg), relative to LMC center (81.24°, −69.73°). Bottom: NIR CMD (J–K_S vs K_S). In both figures, the full photometric data set is displayed as the grayscale background, indicating the stellar density on a logarithmic scale, while the points in red represent the stars with a spectroscopic counterpart, representing the final sample used in this work.

Chapter 3

Data Analysis

After selecting our final sample of 4559 GIRAFFE spectra, I proceeded with the spectral analysis. Before deriving RVs using the penalized pixel fitting (`pPXF`) routine, I cleaned the spectra from the contamination of the sky, following the methodology used in Koch et al. (2007).

3.1 Sky subtraction

An essential procedure in the data analysis was the sky subtraction, as the majority of the spectra of the sample still contained contamination from sky emission lines, which could significantly affect the accuracy of the velocity analysis by introducing noise and distorting the observed stellar spectra.

To address this issue, I used available sky spectra from the ancillary product files, provided by ESO. These files contain spectra from ~ 20 fibers, collected during the same observing periods as the object spectra, ensuring that the sky contribution matched the observational conditions as closely as possible. These spectra were median-combined (using all available sky fibers) to create a median sky spectrum for subtraction. Given that the object spectra are shifted to the heliocentric RV system, while the sky spectra are not, the sky spectrum was aligned with the stellar spectrum by applying a Doppler shift correction based on the heliocentric velocity of the object, using the header keyword `HELICORR`. The corrected wavelength was determined using:

$$\lambda_{\text{cor}} = \left(1 + \frac{v_{\text{helio}}}{c}\right) \times \lambda_{\text{uncor}} \tag{3.1}$$

where c is the speed of light and v_{helio} is the projected heliocentric velocity shift computed by the ESO pipeline for each science spectrum.

The sky spectrum was modeled as the sum of the median sky spectrum and a second-order Legendre polynomial (Eq. 3.3). Additionally, we introduced a small velocity shift in the sky spectrum to ensure proper wavelength calibration relative to the science spectra.

The optimal parameters for both the polynomial and the velocity correction were determined using a Markov Chain Monte Carlo (MCMC) approach, which allowed for a more reliable determination of the best-fitting values. The parameters were optimized using the logarithmic likelihood function:

$$\log L = \sum_{i=1}^{N} \left[\log \frac{1}{\sqrt{2\pi}\sigma} - \frac{(F_{\text{obj}} - F_{\text{sky},i})^2}{2\sigma^2} \right] \tag{3.2}$$

where N is the number of spectral points, F_{obj} is the flux of the object spectrum, and $F_{\text{sky},i}$ is the modeled sky spectrum, defined as:

$$F_{\text{sky},i} = a\lambda^2 + b\lambda + c + F_{\text{median sky}} \tag{3.3}$$

with a, b, c as the free parameters to be determined.

The final sky-subtracted spectrum was obtained by subtracting the Doppler-shifted sky model from the stellar spectrum. The corresponding uncertainty σ was calculated as the quadratic sum of the errors from the object spectrum and the median sky spectrum:

$$\sigma^2 = \sigma_{\text{obj}}^2 + \sigma_{\text{median sky},i}^2 \tag{3.4}$$

Figure 3.1 shows an example of the sky subtraction analysis for a random spectrum, source ADP.2019-04-30T17_31_15.141_111. Figures 3.1(a) and 3.1(b) display the sky spectrum obtained by averaging all spectra from the ~ 20 fibers and the uncorrected object spectrum, respectively. It is evident from the figure that the star spectrum contains emission lines that can affect the analysis for determining the star's RV. Before performing an accurate sky subtraction using a Monte Carlo approach and modeling with Legendre polynomials, a simple subtraction was carried out, as shown in Figure 3.1(c). The graph highlights that, even if the spectrum has indeed improved, the simple subtraction does not completely remove the sky influence. This is particularly noticeable at a wavelength of approximately 630 nm, where a residual emission line is still present. Figure 3.1(d) compares the observed sky spectrum with the sky model obtained using Legendre polynomials, while Figure 3.2 presents the final sky-subtracted and normalized object spectrum for the source `ADP.2019-04-30T17_31_15.141_111`.

3.2 Radial velocity determination: `pPXF`

To derive the radial velocities of the stars in my sample, I performed full-spectrum fitting using the penalized pixel fitting (`pPXF`) routine (Cappellari, 2023). From an observed spectrum, `pPXF` derives RV and velocity dispersion, parameterized via Gauss-Hermite moments and using an approach of maximum penalized likelihood. Traditional methods of RV determination typically rely on a few isolated spectral lines, often resulting in uncertainties due to the limited informa-

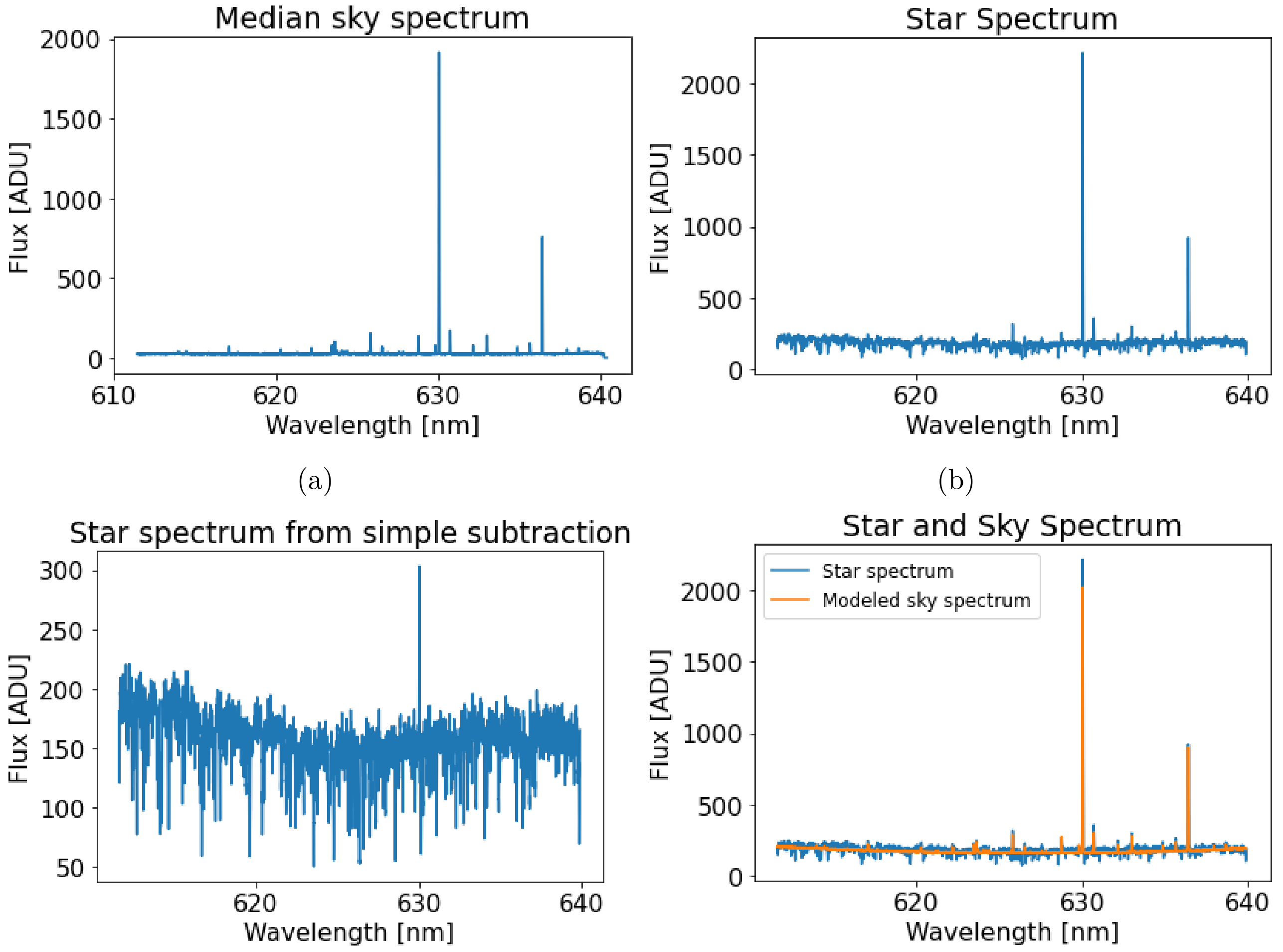

(a) (b)

(c) (d)

Figure 3.1: Steps of the sky subtraction procedure performed for the source ADP.2019-04-30T17_31_15.141_111. (a) Median sky spectrum obtained by averaging the sky fibers. (b) Uncorrected object spectrum before any subtraction. (c) Result after a simple sky subtraction, showing residual contamination. (d) Comparison between the observed star spectrum (blue) and the modeled sky obtained using Legendre polynomials (yellow).

tion used for the fit. In contrast, `pPXF` uses the entire spectral range, making it a more robust and reliable method for determining stellar kinematics. It fits the spectrum with a best-fitting linear combination of differently weighted stellar templates in pixel space.

As templates, I used the X-shooter Spectral Library (XSL) DR2 (Gonneau et al., 2020), a moderate-resolution (R $\sim$ 10 000) spectral library released on January 10th, 2020. The observations were carried out with the X-shooter three-arm spectrograph on ESO's VLT. The XSL DR2 empirical spectra are available in three spectral ranges, corresponding to the three arms of the spectrograph: UVB (300–556 nm), VIS (533–1020 nm), and NIR (994–2480 nm). This dataset contains a comprehensive collection of 813 observations of 666 distinct stars, spanning a broad range of stellar types and conditions, and includes three columns: `WAVE`: Wavelength [in nm], `FLUX`: Flux spectrum [in $\mathrm{erg\,s^{-1}\,cm^{-2}\,^{-1}}$] and `ERR`: Error spectrum: [same units as `FLUX`].

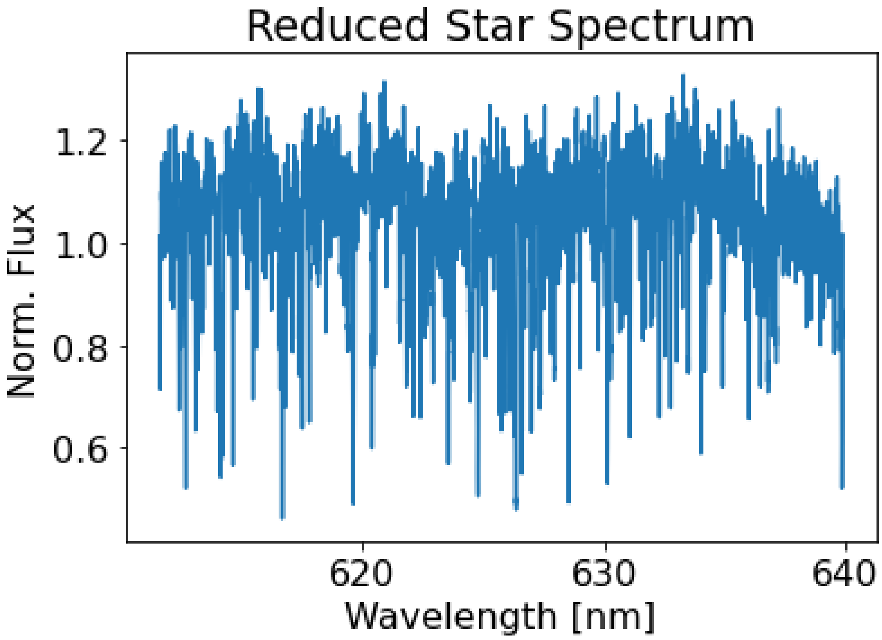

Figure 3.2: Final reduced and normalized spectrum of the source ADP.2019-04-30T17_31_15.141_111 after the sky subtraction using the Monte Carlo approach and Legendre polynomial modeling. The residual sky emission lines have been effectively removed, resulting in a clean stellar spectrum suitable for RV analysis.

Before applying the `pPXF` routine, I preprocessed the observed spectra to ensure that they were in the optimal form for fitting. This preprocessing involved normalizing each spectrum to account for variations in overall flux levels and reducing it to a logarithmic scale using the `log_rebin` function, which facilitates aligning the observed spectrum with the templates by binning the data in log-wavelength space. Afterward, we defined a mask to exclude regions of the spectrum that should be ignored during the fitting process (bad pixels). This was necessary because, even after sky subtraction, some of the spectra still showed contamination from sky emission lines, which could have negatively affected the fitting process. To achieve this, the flux was smoothed using a Gaussian convolution, and the differences between the original and smoothed flux were calculated. This difference was then σ-clipped, selecting all pixels that deviate from the mean by more than 3σ; clipping was performed iteratively until convergence was achieved and no pixels were removed. Additionally, binary dilation was applied to expand the mask (±2 pixels). The identified bad pixels were then excluded from the fitting procedure using the `MASK` keyword in `pPXF`. The templates from the XSL Library were also processed by performing a log-rebinning operation to match the wavelength range of the observed spectrum, normalized to ensure a uniform scale for comparison, and convolved to match the instrumental broadening of the data.

Subsequently, the `pPXF` method was applied to find the best-fitting RV and velocity disper-

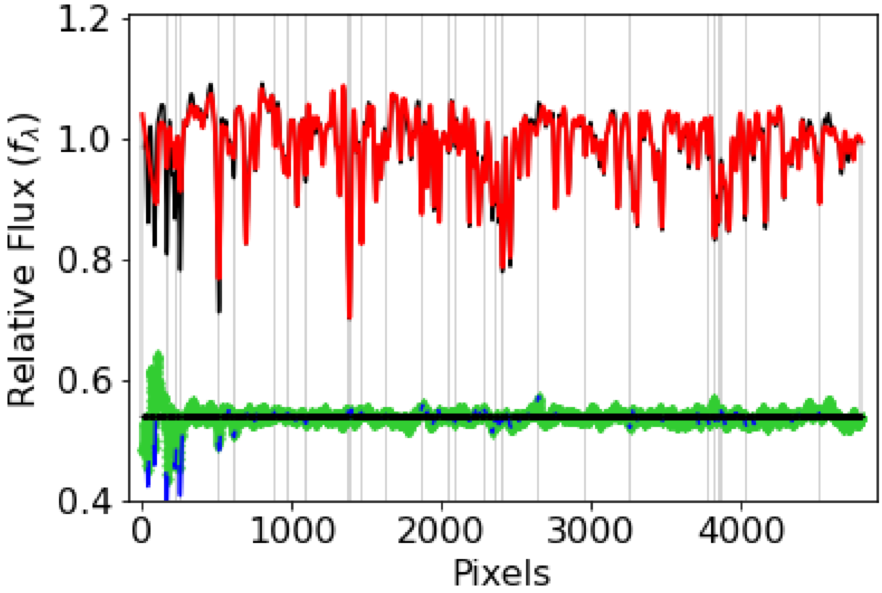

Figure 3.3: `pPXF` example for `ADP.2019-01-29T17_03_02.059`. The reduced spectrum obtained from the sky-subtraction is shown in black, the best-fitting model from `pPXF` in red, and the residuals (data-model) in green. The light vertical lines mark the bad pixels excluded from the fit.

sion for each template by comparing it to the observed spectrum. The fitting was performed by varying the initial starting velocity, which is required by `pPXF`, in discrete steps of 50 km s^{-1} within a range from 0 to 400 km s^{-1}. For each step, the `pPXF` routine was applied to fit the observed spectrum to the stellar template. The best-fit velocity is selected based on the fit residual, ensuring that the standard deviation of the residuals is comparable to their mean, which indicates a good template match.

Figure 3.3 shows the spectra, the spectral fit and the residuals of the source ADP.2019-01-29T17_03_02.059, obtained using `pPXF`. Each fit is the combination of a number of templates at the same RV, listed in Table 3.1 in order of weight, with their associated parameters: effective temperature ($T_{\rm eff}$), surface gravity ($\log g$), and metallicity ([Fe/H]). These templates represent the stellar populations that best reproduce the observed spectrum of ADP.2019-01-29T17_03_02.059. Stars with similar RV do not necessarily share the same atmospheric parameters; the large range of template parameters therefore reflects the diversity of templates contributing to the fit, rather than the atmospheric parameters of a single star. The best-fit RV for this source is $\langle V \rangle = 272.0 \pm 2.3$ km s^{-1}.

HNAME	$T_{\rm eff}$ (K)	$\log g$ (cm/s^2)	[Fe/H]	Weight
HD 213042	4475	4.35	0.09	29.52
HD 58072	5127	2.38	0.03	23.20
HD 141531	4448	1.02	-1.65	11.28
HD 58554	4399	2.07	-0.27	9.70
NGC 6838 1078	4305	2.02	-0.18	9.20
SHV 0523371-713351	3847	1.22	-0.64	4.91
HD 27771	5325	4.62	0.27	4.62
CL* NGC 5904 Arp III-03	4158	1.02	-1.23	3.75
SHV 0520036-692817	3641	1.05	-0.61	1.12

Table 3.1: Stellar templates contributing to the spectral fit of `ADP.2019-01-29T17_03_02.059`. The first column represents the name of the source, while the remaining columns list the effective temperature ($T_{\rm eff}$), surface gravity ($\log g$), metallicity ([Fe/H]), and the relative weight of each template. Templates contributing less than 1% were excluded from this table.

Chapter 4

Results & Discussion

In this chapter, I present the results of my study, beginning with the analysis of radial velocity in the LMC. Next, I compare my findings with external datasets from the literature and examine how radial velocities differ among various stellar populations by analyzing different regions in the CMD.

4.1 Radial velocities: data quality and final sample

After finishing the analysis described in Chapter 3, I examined the RV measurements for my sample of stars. During the analysis, however, some sources could not be processed due to various reasons. In some cases, sky spectra were missing, and thus the subtraction was not possible, leading to their exclusion from the sample. For others, `pPXF` gave errors, most likely due to problematic spectra or negative flux values at the edges that were not fully removed. When such issues happened, the script simply moved on to the next object without producing results.

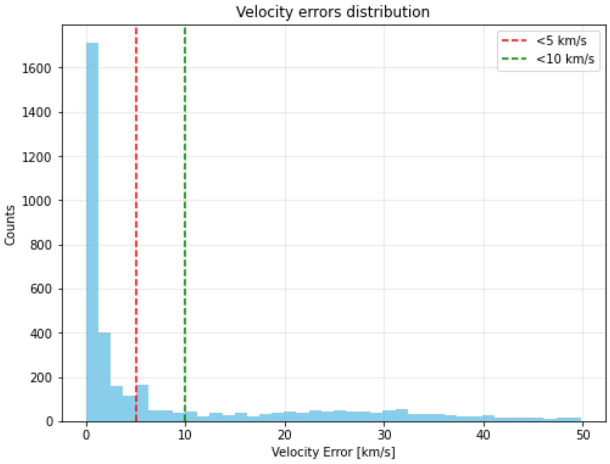

Figure 4.1: Distribution of RV errors (in km s^{-1}) for the sample of stars analyzed. Most stars exhibit errors lower than 5 km s^{-1}, as highlighted by the red dashed line, while the green dashed line marks the 10 km s^{-1} threshold.

In the end, I successfully measured the radial velocities of 4,310 stars. Among these, some exhibited very large errors, likely due to failed sky subtraction, in which prominent sky lines remained in the spectrum, leading to poor fits with large residuals. Specifically, 4,010 stars (93%) had radial velocity errors (V_{err}) below 50 km s^{-1}. The 295 stars with errors of 50 km s^{-1} or greater were excluded from further analysis. As Figure 4.1 shows, most of the retained sample has V_{err} below 10 km s^{-1}.

4.1.1 The Carina Dwarf Spheroidal Galaxy

During the analysis of the sky distribution, I noticed a group of stars concentrated in the upper right region, which resembles a cluster or an overdensity, highlighted in blue in panel (a) of Figure 4.2.

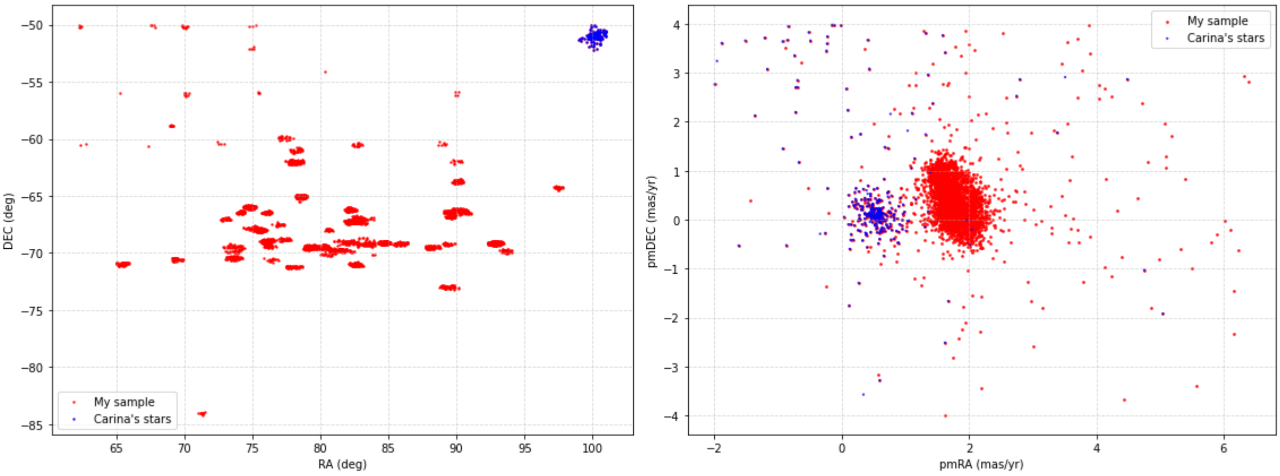

(a) (b)

Figure 4.2: Spatial distribution (a; RA vs Dec) and proper motion diagram (b; μ_{RA} vs μ_{Dec}) of the stars in my sample (red), and the stars in the found overdensity (blue).

To investigate further, I projected this "cluster" onto the proper motion diagram and found that these stars displayed values distinct from those typical of the LMC population (panel (b) in Fig. 4.2). Examining their sky position, we conclude that this group corresponds to the Carina dwarf spheroidal galaxy (dSph), 100 kpc away from the Sun (van den Bergh, 2000), discovered by Cannon et al. (1977) at a location of: RA = 100.4°, Dec = -50.97°, perfectly matching our overdensity.

Figure 4.3 shows the histogram of the radial velocity distribution of this group of stars. They exhibit lower velocities than the ones typical of LMC stars, another indication that the group doesn't belong to the Large Cloud. Taking into account only sources exhibiting a velocity between 152 and 270 km s^{-1} (corresponding to the $\pm 3\sigma$ of the peak), the mean velocity is $\langle V \rangle = 216 \pm 1$ km s^{-1}, with a velocity dispersion of $\sigma = 11 \pm 1$ km s^{-1}. This value is consistent with measurements reported in the literature. For instance, Fabrizio et al. (2011) measured a

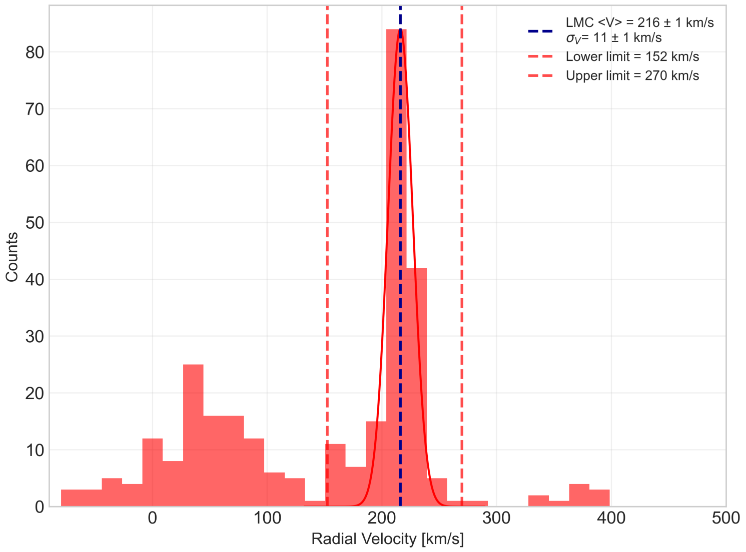

Figure 4.3: Histogram of the RV distribution of stars in the Carina dSph. The bin width is 18 km s^{-1}. The red dashed lines mark the lower and upper velocity limits for Carina dSph membership, while the blue one shows the mean RV. The peak at lower velocities represents MW stars.

mean RV of Carina dSph stars to be 220.4 ± 0.1 km s^{-1} and the dispersion of 11.7 ± 0.1 km s^{-1} from a large FORS2+GIRAFFE spectroscopic survey of stars of all evolutionary stages. The identification of Carina dSph is further confirmed by the proper motion values found in this study, consistent with their belonging to the Carina galaxy (Battaglia et al., 2022), rather than to the LMC. Additionally, the majority of the contamination of MW stars in our sample, shown in Fig. 4.3 with a peak at ~ 30 km s^{-1}, comes from this group of stars.

These 310 stars were therefore removed from the sample, significantly reducing the fraction of MW stars.

4.1.2 Radial velocities in the LMC

After removing Carina's stars, the final sample contains 3713 stars. Their RV distribution is displayed in Figure 4.4. To minimize foreground contamination, I first visually identified a preliminary kinematic peak in the range 170–360 km s^{-1}, to which a Gaussian was fitted, yielding initial parameters $V_0 = 271$ km s^{-1} and $\sigma_0 = 31$ km s^{-1}. The final LMC sample was then defined as all stars within $\pm 3\sigma$ of this peak ($178 < V < 364$ km s^{-1}). The velocity histogram of this clean sample was fitted with a Gaussian function, resulting in a mean radial velocity of $\langle V \rangle = 273 \pm 1$ km s^{-1} and velocity dispersion $\sigma_V = 31 \pm 1$ km s^{-1}.

We proceeded with the analysis by visualizing how the velocity changes on the color-magnitude, spatial distribution, and proper motion diagrams, as shown in Figure 4.5. To give a better idea of where the stars lie in the galaxy, Fig. 4.6 also shows the spatial distribution of our LMC stars using the same coordinates transformation used in Fig.2.3(a), with a background density

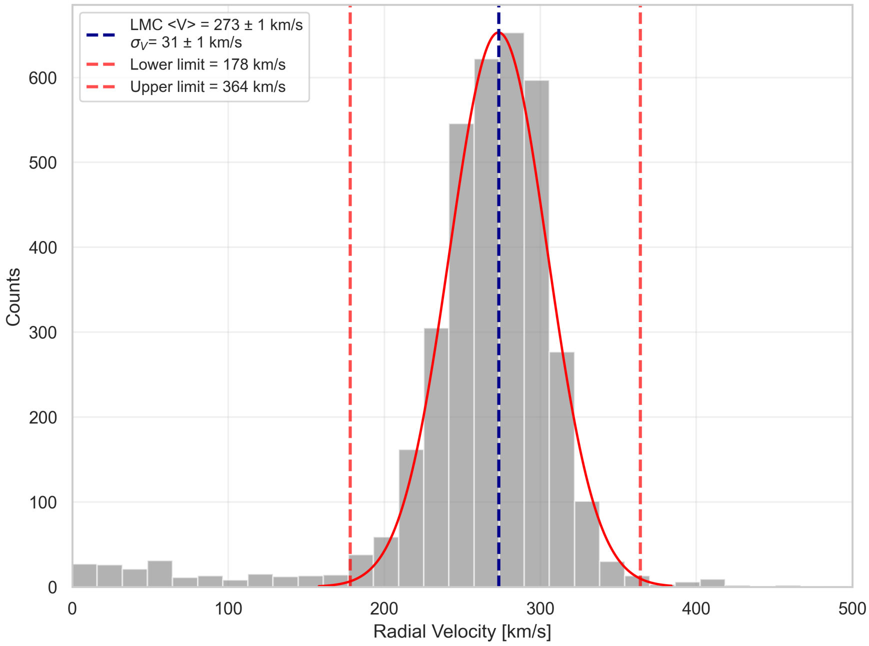

Figure 4.4: Histogram showing the RV distribution of the stars in my sample. The selection limits, 178 km s^{-1} and 364 km s^{-1}, indicated by the red dashed lines, correspond to the $\pm 3\sigma$ range around the fit. The mean velocity of 273 ± 1 km s^{-1} is highlighted by the blue dashed line. The bin width is 16 km s^{-1}.

map from the photometric parent sample derived at the beginning of the sample selection process, containing around 3 million stars. As visible in panel (a) of Figure 4.5 and Figure 4.6, a clear gradient in radial velocity can be observed across the galaxy. Stars in the south-western regions of the system show lower radial velocities, while those on the opposite side exhibit higher velocities. This systematic variation reflects the expected kinematics of a rotating disk galaxy, where different regions of the disk move toward or away from the observer due to the galaxy's rotation.

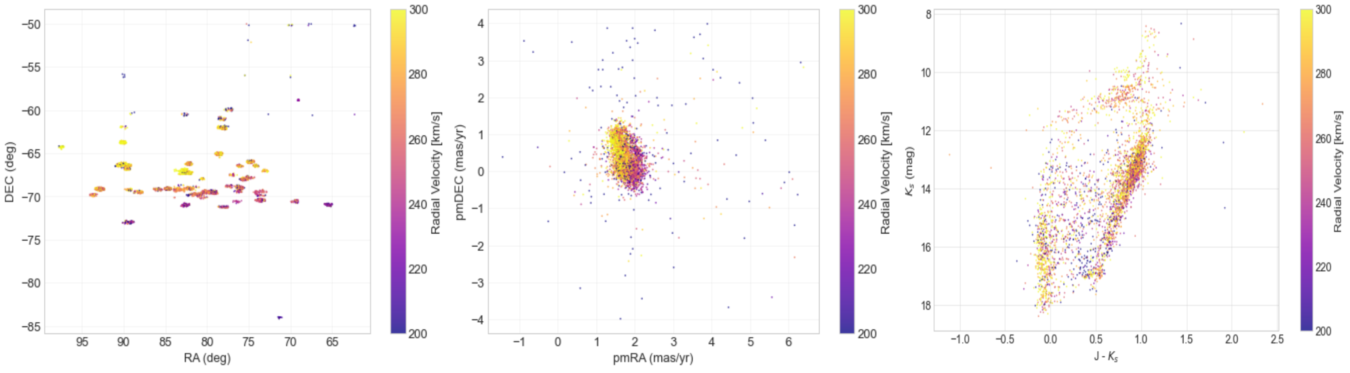

(a)

(b)

(c)

Figure 4.5: Spatial distribution (a), proper motion diagram (b), and CMD (c) of the sample, color-coded based on their radial velocity.

Our results are validated further by Gaia DR3 kinematic studies of the LMC (Katz et al., 2023), who studied the radial velocities of 29,631 AGB and blue loop stars (stars which deviate from the RGB and form a loop toward the bluer side of the Hertzsprung-Russell diagram). Fig. 4.7 shows the distribution of stars in their sample, color-coded according to their combined radial velocities. They exhibit the same clear gradient, from ∼320 km s^{-1} (red) at the top to ∼200 km s^{-1} (blue) at the bottom, which maps the rotation of the LMC projected onto the line of sight.

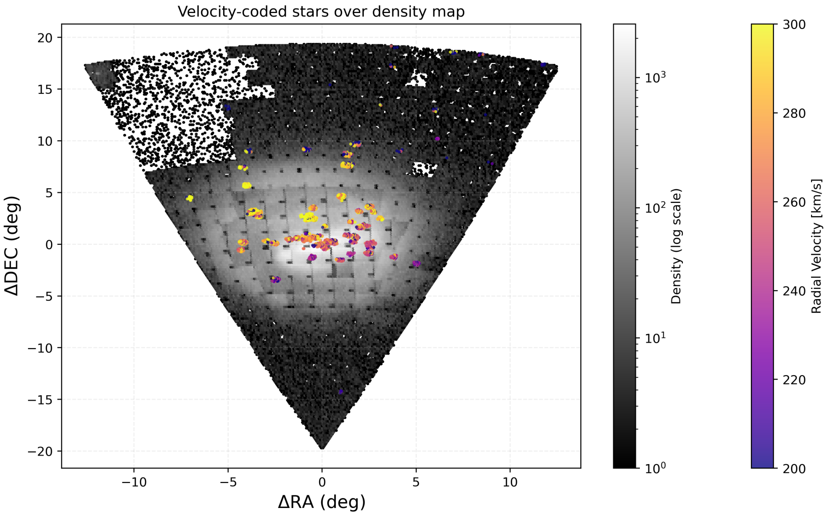

Figure 4.6: Velocity-coded over density map of stars in the LMC. Stars are color-coded by their RV. The gray-scaled background shows the photometric sample.

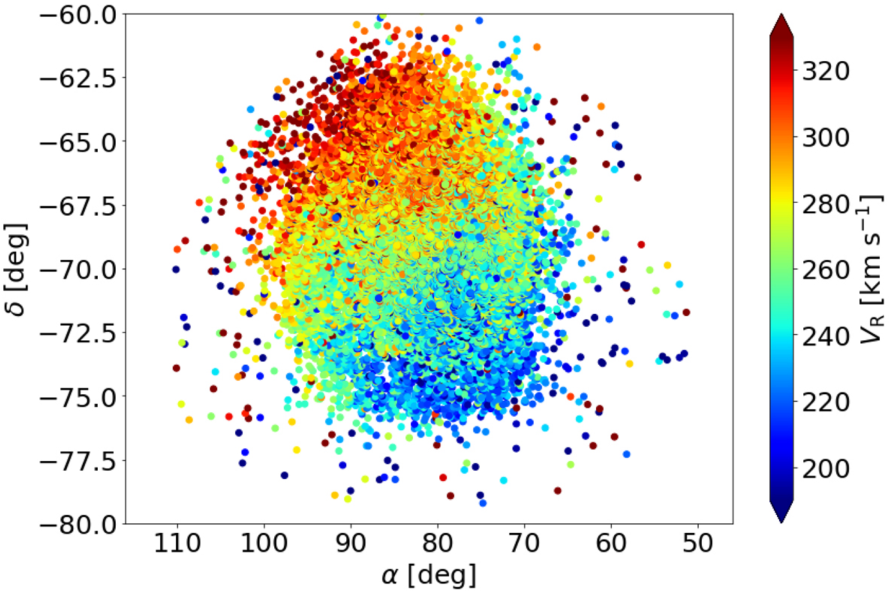

Figure 4.7: Distribution of a sample of 29,631 AGB and blue loop stars in the LMC from Katz et al., 2023 (Figure 17), color-coded by combined radial velocities. The axes represent right ascension (α, RA) and declination (δ, Dec).

4.2 Comparison with the literature

The radial velocities derived in this work were compared with measurements from the Sloan Digital Sky Survey (SDSS) and Gaia surveys to validate their reliability.

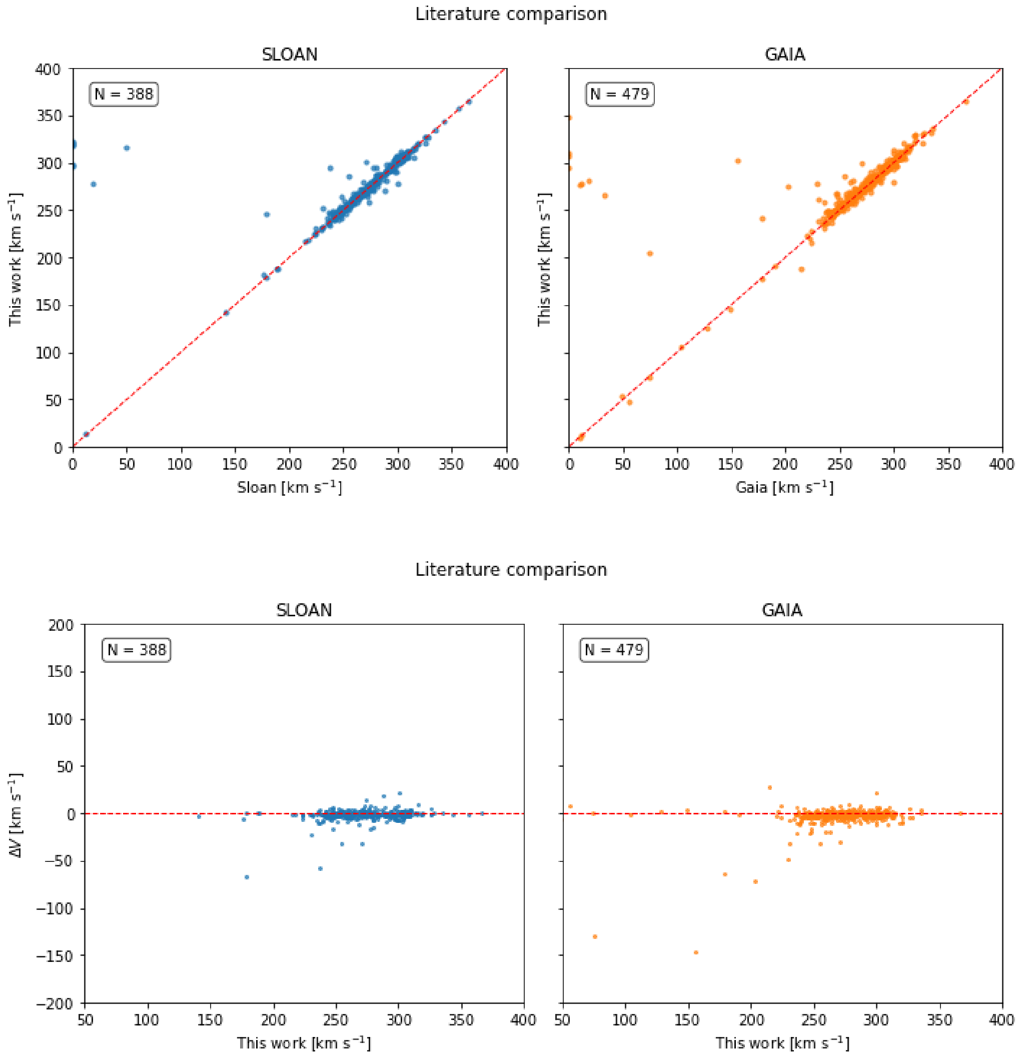

Figure 4.8: Comparison between the radial velocities measured in this work and values from SDSS and Gaia. In all panels, N denotes the number of sources in our sample with a counterpart in the respective survey. Top: the red dashed line indicates the one-to-one relation, where the majority of stars lie. Bottom: ΔV (velocity difference between our sample and the reference survey) shows no offset, being centered around zero.

The SDSS is a large sky survey, carried out with the dedicated 2.5-meter wide-angle optical telescope located at Apache Point Observatory, New Mexico (USA). It is one of the most challenging and influential ground-based surveys to date, having cataloged approximately 100 million stars, 1 million galaxies, and 100,000 quasars, and providing both photometric and spectroscopic observations.

In the SDSS project, the incoming light is alternately directed to two instruments: the first is a multi-filter/multi-array scanning CCD camera, designed to take an imaging survey of the sky at high efficiency in ultraviolet, green, red, and infrared. The second instrument consists of a pair of spectrographs that can take spectra of several hundred (over 600) objects at a time.
For our comparison, we use data from the latest SDSS-IV data release, DR17, which provides high-resolution NIR spectra for hundreds of thousands of stars, along with precise radial velocities and associated uncertainties. The imaging survey covers 14,555 square degrees, corresponding to about one-third of the sky, while the spectroscopic portion includes detailed measurements of more than three million astronomical objects.
As for Gaia, we used the catalog that was used to exclude MW stars in the sample selection.

The results of the comparison are displayed in Figure 4.8. Only a limited number of stars (~ 500 for Gaia and ~ 400 for SDSS) had a radial velocity value. For both catalogs, the majority of stars lie close to the one-to-one relation, indicating good overall agreement between our measurements and the literature. The few outliers, which show lower velocities in the literature catalogs compared to our measurements, might reflect an underestimation of radial velocities in those surveys, given that our velocities for these outliers remain consistent with the LMC mean velocity. The residuals ΔV, defined as the velocity difference between our sample and the reference survey, are centered around zero, and show no strong trends with velocity, indicating no significant systematic offset with respect to the reference survey.

4.3 Stellar populations

To investigate how kinematics vary across different stellar populations, the CMD was divided into distinct regions corresponding to the main evolutionary sequences, following the classification adopted in Cioni et al. (2014). To better match our data, we added region M, comprising thermally pulsing AGB stars, and extended regions with fainter stars down to K_S=19 and those with brighter stars up to K_S=10, as done by El Youssoufi et al. (2019). The boundaries of every region used in this project are listed in the Appendix, Table A.1, and a visual representation is shown in Fig. 4.9, which displays the CMD (J-K_S vs K_S) color-coded by region.

Regions A, B, C, and D consist of main sequence stars but with different ages. The first three are all young stellar populations ($\sim 20 \pm 15$ Myr, $\sim 195 \pm 206$ Myr, $\sim 891 \pm 739$ Myr, respectively), while region D represents a population of main sequence and/or subgiant stars with a median age of $\sim 2.45 \pm 1.53$ Gyr. Region E corresponds to lower RGB stars with a median age of $\sim 3.72 \pm 2.48$ Gyr. Region F is primarily populated by MW foreground stars, but is only weakly represented in our sample. Region G consists of blue supergiants and giant stars with a median age of $\sim 81 \pm 39$ Myr. Region H represents a population of red supergiants and giant stars with a median age of $\sim 170 \pm 59$ Myr and contains most of the Cepheids. Re-

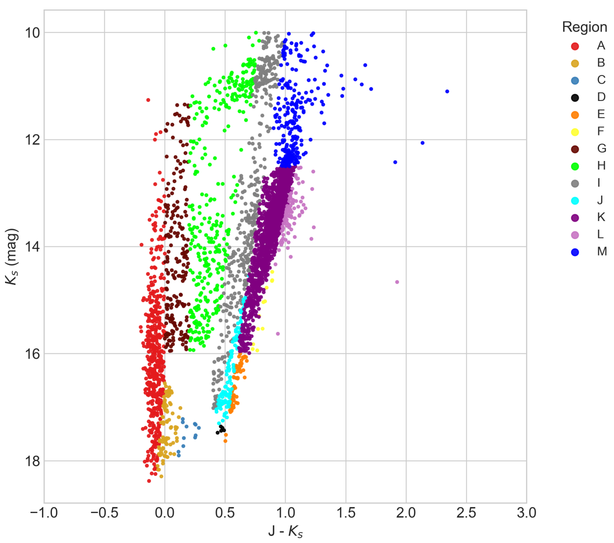

Figure 4.9: CMD of the stellar sample, color-coded according to the regions (A–M). Regions A–D trace main-sequence stars of increasing age. Regions E, J, and K correspond to red giant and red clump stars of intermediate and old ages. Regions G, H, and I contain blue, red, and yellow supergiants and giants, respectively, while region M marks thermally pulsing AGB stars. Region L traces galaxies, while Region F is mainly associated with MW stars.

gion I marks yellow supergiants and giant stars, with an age of $\sim 446 \pm 257$ Myr. Region J is dominated by the intermediate-age RC population, but also includes old horizontal and red giant branch stars, resulting in a median age of $\sim 3.71 \pm 3.42$ Gyr. Region K, located above the RC, is our most populated region, and corresponds to the upper RGB stars with a median age of $\sim 3.23 \pm 2.16$ Gyr. Lastly, region M represents the thermally pulsing AGB population with a median age of $\sim 2.45 \pm 1.58$ Gyr. Region L is mostly populated by galaxies, thus we exclude it from the analysis.

For each region, we computed the mean velocity $\langle V \rangle$ and velocity dispersion σ_v using the same Gaussian-fitting procedure applied to the full sample (Section 4.1.2). The results are shown in Table 4.1, whose columns include the number of sources, the mean RV, and velocity dispersion (with associated errors) for each region, while the histograms of their radial velocity distribution are displayed in the Appendix (Fig. A.1 and A.2). Excluding regions C, D and F, which contain too few stars for a reliable kinematic analysis (N = 11, 3 and 12, respectively), the majority of the regions exhibit mean radial velocities between about 265 and 285 km s^{-1}.

The most problematic region is Region E (N = 48), which contains lower RGB stars with an age range of 1.24-6.20 Gyr. While its mean velocity (275 km s^{-1}) is consistent with the other regions, it shows an extremely low velocity dispersion of 4.6 km s^{-1} and unusually large uncertainties, of the order of 40 km s^{-1} for both parameters. This indicates that the velocity distribution is poorly described by a Gaussian profile (see panel (a) in Fig. 4.10). Figure 4.10

Table 4.1: Summary table of the kinematic properties of the stars in my sample, divided by regions in the CMD. N is the number of stars in each region. $\langle V \rangle$, V_{err}, σ, and σ_{err} are the mean RV, its associated uncertainty, the velocity dispersion, and its uncertainty, respectively, all expressed in km s^{-1}. Age ranges are reported in Myr for young populations and in Gyr for older populations. We excluded regions with $N < 15$ and region L, which is populated by galaxies.

Region	N	$\langle V \rangle$	V_{err}	σ	σ_{err}	Age range
A	444	291.2	2.7	24.6	2.7	5–35 Myr
B	80	274.8	1.5	28.5	1.5	0–401 Myr
G	183	265.8	1.0	32.3	1.0	42–120 Myr
H	306	268.8	1.4	30.5	1.4	111–229 Myr
I	321	272.6	0.9	25.4	0.9	189–703 Myr
E	48	274.6	40.0	4.6	34.7	1.24–6.20 Gyr
J	101	276.7	4.2	32.6	4.2	0.29–7.13 Gyr
K	1404	271.0	0.7	31.4	0.7	1.07–5.39 Gyr
M	251	282.1	0.5	28.7	0.5	0.87–4.03 Gyr

also shows the histogram of velocities of Region K (upper RGB star), the most populated one. While Region E shows a less regular distribution with larger uncertainties, Region K shows a symmetric distribution that is closely approximated by a Gaussian profile. These two examples are presented here to illustrate a contrast between a low-statistics, poorly constrained distribution and a high-statistics case where the Gaussian model provides an excellent description of the data.

Given that the goal of this analysis is to investigate how radial velocity varies with stellar age, I decided to combine Region E and J into a single sample. They correspond to the RC and lower RGB, share a similar mean velocity ($\sim$275 km s^{-1}), and, most importantly, their age ranges are comparable, which supports treating them as a single population. The resulting velocity distribution appears closer to a Gaussian profile (see Fig. A.2, Region E+J in the Appendix), and the associated uncertainties decrease significantly.

We further examine the dependence of mean RV on stellar age in Figure 4.11, where the average RV of different stellar populations is plotted as a function of their age (in logarithmic scale), with vertical and horizontal error bars representing the uncertainties on $\langle V \rangle$ and the age ranges, respectively. When it comes to mean radial velocity, there is one clear outlier, region A, which exhibits a notably high value of 291 km s^{-1} relative to all other regions. A plausible interpretation of this is that the stars in Region A formed from gas that had been accelerated during a past dynamical interaction. Such an event may have generated high-velocity gas clouds, whose kinematics were subsequently inherited by the newly formed stars.

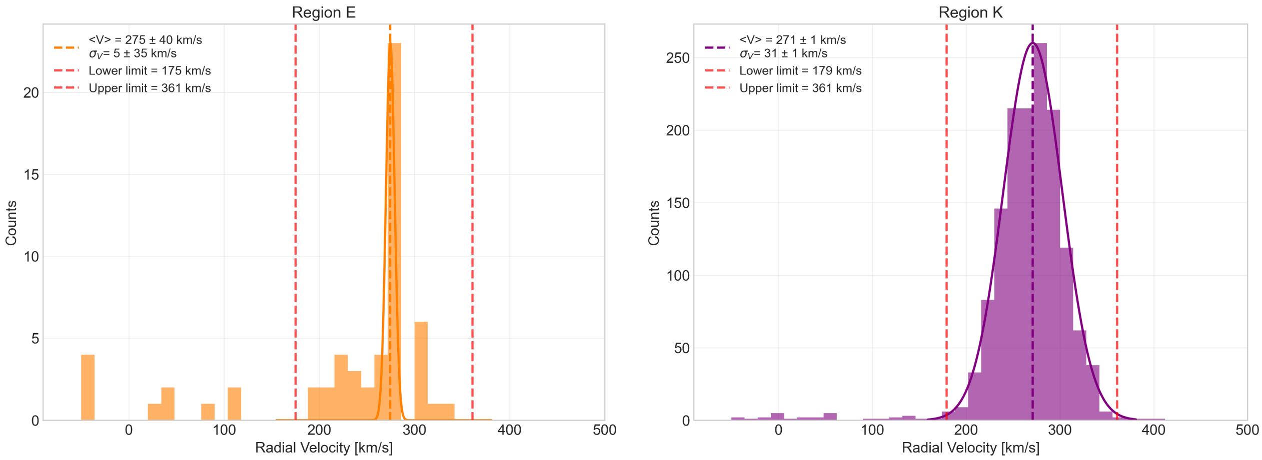

(a) (b)

Figure 4.10: RV distributions of two representative regions, with a bin size of 14 km s^{-1}. Panel (a): Region E, showing a low-statistics sample with a non-Gaussian distribution and large uncertainties. Panel (b): Region K, whose velocity distribution is symmetric and well described by a Gaussian profile.

Interestingly, Region G, whose stellar population has a similar age to Region A, exhibits the lowest mean velocity in the sample (266 km s^{-1}). To try to understand the reason behind this unexpected significant difference, we looked into their spatial distribution, shown in Fig. 4.12. The high-velocity stars of Region A appear to be concentrated in an area consistent with Shapley Constellation III (SC III), located at $\Delta\mathrm{RA} \approx -1°$, $\Delta\mathrm{DEC} \approx 2.5°$, a super-giant shell of HI, where multiple recent episodes of star formation have been documented (e.g. Harris & Zaritsky, 2008). Dopita et al. (1985) reported a disk H I component with a mean velocity of $\sim$285 km s^{-1} in this region, consistent with the high velocity measured for Region A. While both regions exhibit a similar velocity gradient in the central parts of the galaxy, Region G contains fewer stars associated with SC III, and those present display relatively low radial velocities. This may suggest that these stars formed before the event that accelerated the gas cloud, and thus did not inherit the high-velocity kinematics observed in Region A. However, the limited number of stars available prevents us from drawing firm conclusions.
The spatial distributions of the individual regions, color-coded according to their radial velocities, are presented in Fig. A.3, A.4, and A.5 in the Appendix A.

Lastly, we compared the old ($\geq$ 1 Gyr) and young ($\leq$ 1 Gyr) populations to search for possible global trends in the kinematics. The young population comprises regions A, B, G, H, and I, whereas the old population includes regions E, J, K, and M. The results are listed in Table 4.2, and the histograms representing their different radial velocity distributions are shown in Fig. 4.13. Overall, the two populations display very similar kinematic properties. The young population, consisting of 1,181 stars, has a mean radial velocity of 276 km s^{-1}, while the old population shows a mean value of 273 km s^{-1}. In addition, both populations exhibit compara-

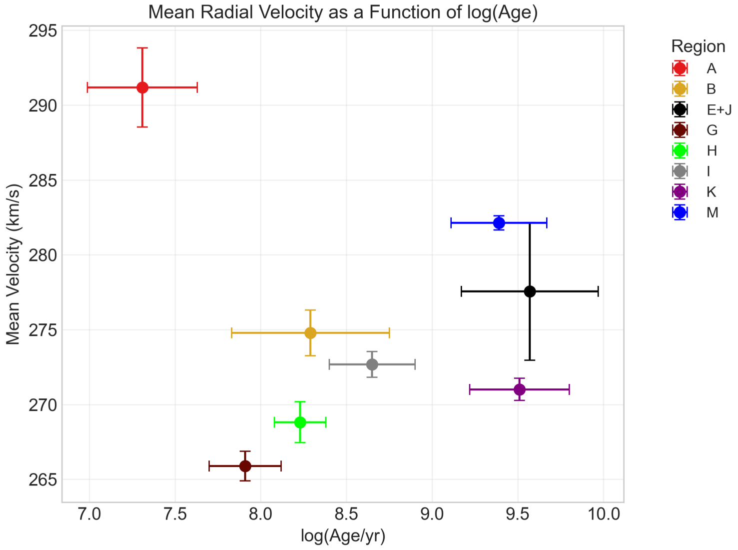

Figure 4.11: Mean RV of stars as a function of their age in logarithmic scale for different regions in the sample. Each point represents the average velocity in a region, with vertical error bars showing the uncertainty on the mean and horizontal error bars indicating the age ranges. Colors distinguish the regions A, B, G, H, I, K, M, and the combined region E+J.

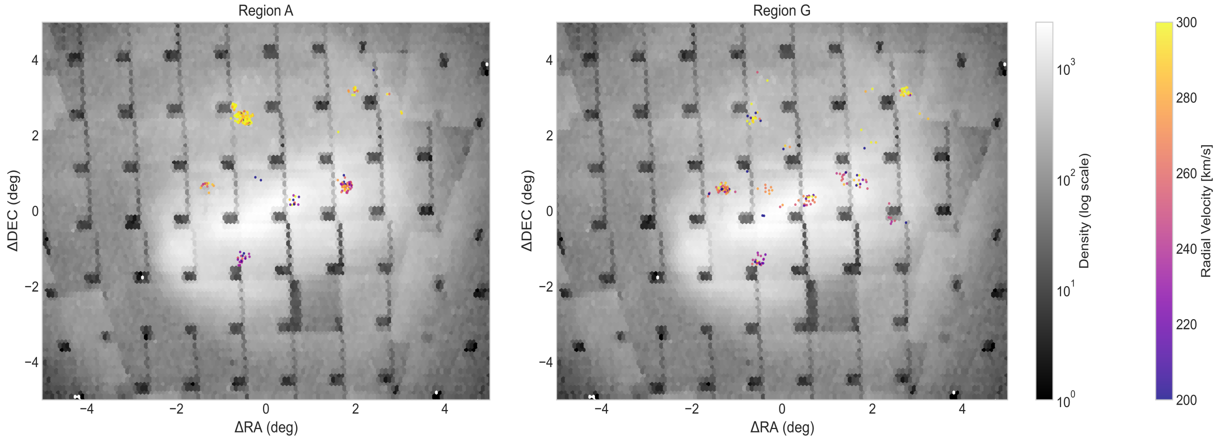

(a)

(b)

Figure 4.12: Velocity-coded over density map of stars in Regions A (a) and G (b). The gray-scaled background is once again the full photometric sample. Both regions host young populations (age ∼ 15–80 Myr, Table 4.1).

ble velocity dispersions, indicating no significant kinematic separation between young and old stars, within the limits of our sample.

Table 4.2: Kinematic properties of the young (< 1 Gyr) and old (> 1 Gyr) stellar populations. N is the number of stars in each population, $\langle V \rangle$ is the mean radial velocity, σ_V is the velocity dispersion, and the last column indicates the CMD regions included in each group.

Population	N	$\langle V \rangle$ [$\mathrm{km\,s^{-1}}$]	σ_V [$\mathrm{km\,s^{-1}}$]	Regions
Young	1181	275.8 ± 1.3	31.4 ± 1.3	A, B, G, H, I
Old	1826	273.2 ± 0.8	31.2 ± 0.8	E, J, K, M

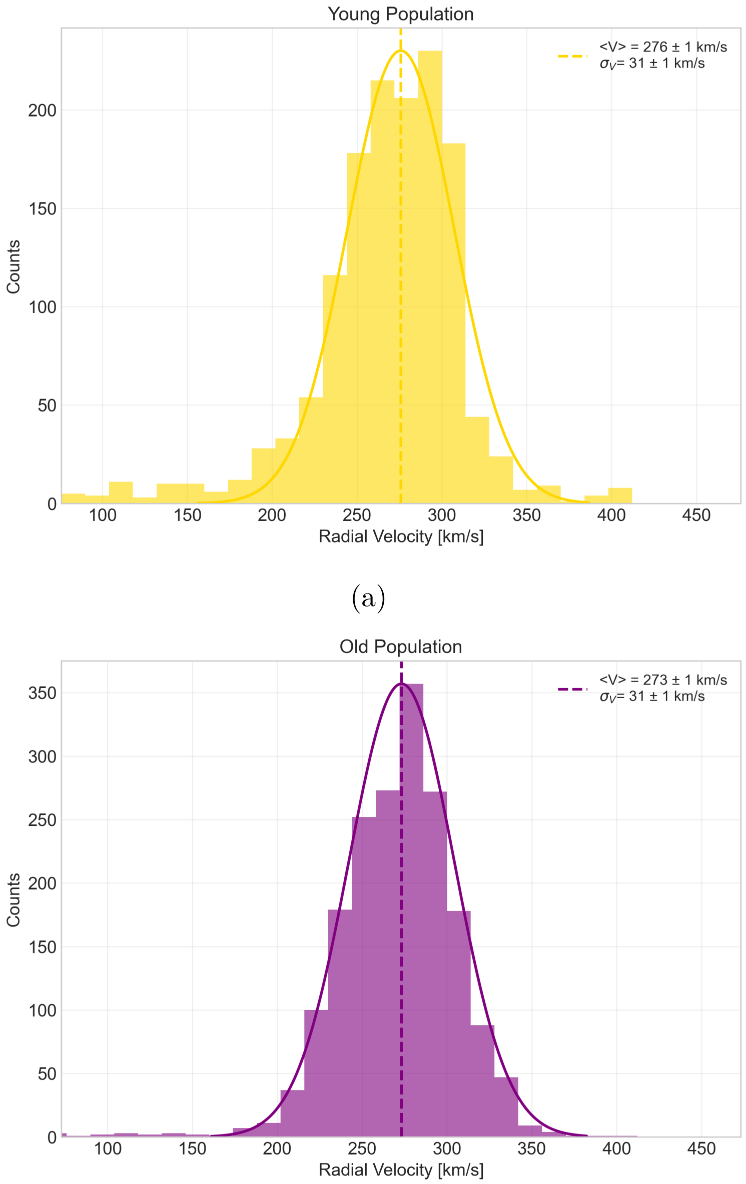

(a)

(b)

Figure 4.13: Comparison of the velocity distributions for the young population (top; regions A, B, G, H, and I) and the old population (bottom; regions E, J, K, and M), showing very similar mean velocities and dispersions. The bin size is 14 km s^{-1}.

Chapter 5

Conclusion

The Large Cloud is one of the most studied galaxies in the Universe, due to its proximity to our Milky Way and the opportunity to resolve individual stars in it. In this thesis, I analyzed a sample of around 4000 stars to derive their radial velocities and to investigate the kinematic properties of different stellar populations in the LMC.

I began by constructing a clean photometric sample within 20 degrees of the optical center of the LMC (81.24°, −69.73°), using NIR magnitudes from the VMC and VHS surveys, complemented at the bright end by 2MASS. A series of quality cuts on morphology and photometric flags was applied, as well as on photometric uncertainties, to ensure that only sources with robust measurements were included in the final catalog. The majority of foreground contamination from the MW was removed using Gaia DR3 parallaxes and proper motions cuts ($\omega < 0.2$, $-2.5 < \mu_{RA} < 6.5$ and $-4 < \mu_{Dec} < 4$). Variable stars were excluded using OGLE-III and OGLE-IV to avoid the impact of pulsation-induced velocity variations on our analysis. The resulting photometric catalog contains more than 3 million sources and serves both as the parent sample for the spectroscopic cross-match and as a reference background for the spatial distribution plots, providing a visual context for the location and extent of the galaxy on the sky. Spectroscopic data were retrieved from the ESO Science Archive Facility, focusing on FLAMES/GIRAFFE spectra with SNR > 10. For each source, a single spectrum was selected, prioritizing higher-resolution, higher-SNR spectra when multiple observations were available.

To make sure that they were in optimal condition for the following analysis, the spectra were cleaned of sky emission lines. I used available sky spectra from the ancillary product files, which were obtained from fibers assigned to capture sky contributions. These fibers were combined to create a median sky spectrum, and then aligned it with the stellar spectra by applying a Doppler shift based on the object's heliocentric velocity. The sky spectrum was modeled as the sum of the median sky spectrum and a second-order Legendre polynomial. A small velocity shift was also applied to optimize the alignment. To determine the optimal parameters for the polynomial and velocity correction, a Markov Chain Monte Carlo approach was employed. The final sky-subtracted spectrum was obtained by subtracting the Doppler-shifted sky model from the stellar spectrum, and the corresponding uncertainty was calculated as the quadratic sum of the errors from the object spectrum and the median sky spectrum.

Radial velocities were then derived using full-spectrum fitting with the `pPXF` routine and templates from the X-shooter Spectral Library. Since `pPXF` requires an initial guess for V_{start}, we implemented a Python cycle that, for each star, calculated the velocity and velocity dispersion by iterating V_{start} from 0 to 400 km s^{-1}. We selected the final velocity as the one that yielded the smallest residuals, ensuring that the residuals' standard deviation was comparable to their mean, indicating a good template match.

After quality cuts on velocity uncertainties, radial velocities of $\sim$ 4000 stars were used for our analysis. The analysis of the spatial distribution revealed a distinct overdensity in the north-western part of the RA–Dec diagram, whose proper motions, sky position, and radial velocities are incompatible with the LMC and are more consistent with the Carina dwarf spheroidal galaxy, instead. For stars in this overdensity, a mean radial velocity of $\langle V \rangle = 216 \pm 1$ km s^{-1} and $\sigma = 11 \pm 1$ km s^{-1} were found, in excellent agreement with previous determinations of the systemic velocity of Carina dSph. Removing these stars led to a final LMC sample of 3713 sources.

The radial velocity distribution of this final sample shows a well-defined peak that can be described by a Gaussian, with LMC members selected within $\pm 3\sigma$ around the fitted mean. Using this selection, the mean radial velocity of the LMC sample is $\langle V \rangle = 273 \pm 1$ km s^{-1}, corresponding to a velocity dispersion of $\sigma_V = 31 \pm 1$ km s^{-1}.

Studying the radial velocities in the RA vs Dec map, we found a clear gradient across the galaxy: stars on the north-eastern side exhibit higher RVs compared to those on the south-western regions, reflecting the expected kinematics of galaxies such as the LMC, where stars move differently due to the disk's rotation.

As validation of our results, we compared our finding with two external catalogs (SDSS and Gaia). Most stars lie close to the one-to-one relation between the velocities measured in this thesis and those from both catalogs.

To try to connect the kinematic properties with stellar ages, we divide the CMD into regions corresponding to different evolutionary stages. The regions are divided as follows: regions A, B, C, and D represent main sequence stars of increasing age, ranging from $\sim 20 \pm 15$ Myr to 891 ± 739 Myr. Region G is a young population of blue supergiants and giant stars. Region E traces lower RGB stars ($\sim 3.72 \pm 2.48$ Gyr). MW foreground stars primarily populate region F. Region H includes red supergiants and giants ($\sim 170 \pm 59$ Myr), while Region I contains yellow supergiants ($\sim 446 \pm 257$ Myr). Region J is dominated by the RC population, with contributions from RGB stars ($\sim 3.71 \pm 3.42$ Gyr). Region K corresponds to the upper RGB ($\sim 3.23 \pm 2.16$ Gyr) and is the most populated in our sample. Region M traces AGB stars ($\sim$

2.45 ± 1.58 Gyr), whereas Region L is mainly composed of galaxies.

Comparing the mean velocities of the different stellar populations, excluding poorly populated regions, we find that most of them show similar values, with values between 265 and 285 km s^{-1}, with the exception of Region A, with a $\langle V \rangle$ of 291 km s^{-1} . What immediately stands out, however, is that the two youngest regions (A and G) display the highest and the lowest mean velocities in the sample, which is somewhat unexpected. The fastest stars in region A are concentrated in a small region of the sky that is spatially associated with the known star-forming complex Shapley Constellation III, where a disk H I component has been reported with a mean velocity of ~ 285 km s^{-1}. These stars could have formed in a recent burst of star formation from gas that was already dynamically accelerated during a past dynamical event, and inherited the velocity of the parent cloud, whereas stars that formed earlier exhibit lower velocities. However, it is difficult to draw firm conclusions because Region G in SCIII contains only a small number of stars, even though some of them do appear to have lower velocities.

A comparison between young (≤ 1 Gyr) and old (≥ 1 Gyr) stellar populations shows no significant differences in their global kinematic properties. The young population has a mean RV of 276 km s^{-1}, whereas the old population has a mean of 273 km s^{-1}. Both groups exhibit the same velocity dispersion of 31 km s^{-1}, indicating that, within the uncertainties of our sample, the overall kinematics of the LMC does not show a clear dependence on stellar age.

Bibliography

Bagheri, G., Cioni, M.-R. L., & Napiwotzki, R. 2013, *Astronomy & Astrophysics*, 551, A78, doi: 10.1051/0004-6361/201118236

Barger, K. A., Madsen, G. J., Fox, A. J., et al. 2017, *The Astrophysical Journal*, 851, 110, doi: 10.3847/1538-4357/aa992a

Battaglia, G., Taibi, S., Thomas, G. F., & Fritz, T. K. 2022, *Astronomy & Astrophysics*, 657, A54, doi: 10.1051/0004-6361/202141528

Besla, G., Kallivayalil, N., Hernquist, L., et al. 2010, , 721, L97, doi: 10.1088/2041-8205/721/2/L97

—. 2012, *Monthly Notices of the Royal Astronomical Society*, 421, 2109, doi: 10.1111/j.1365-2966.2012.20466.x

Brüns, C., Kerp, J., Staveley-Smith, L., et al. 2005, *Astronomy & Astrophysics*, 432, 45, doi: 10.1051/0004-6361:20040321

Cannon, R. D., Hawarden, T. G., & Tritton, S. B. 1977, *Monthly Notices of the Royal Astronomical Society*, 180, 81P, doi: 10.1093/mnras/180.1.81P

Cappellari, M. 2023, MNRAS, 526, 3273, doi: 10.1093/mnras/stad2597

Cioni, M.-R. L., & et al. 2023, VizieR Online Data Catalog: VISTA Magellanic Survey (VMC) catalog (YJKs) DR6 (Cioni+, 2011), VizieR On-line Data Catalog: II/375. Originally published in: 2011A&A...527A.116C

Cioni, M. R. L., Habing, H. J., & Israel, F. P. 2000, *Astronomy & Astrophysics*, 358, L9, doi: 10.48550/arXiv.astro-ph/0005057

Cioni, M. R. L., Clementini, G., Girardi, L., et al. 2011, *Astronomy & Astrophysics*, 527, A116, doi: 10.1051/0004-6361/201016137

Cioni, M.-R. L., Girardi, L., Moretti, M. I., et al. 2014, *Astronomy & Astrophysics*, 562, A32, doi: 10.1051/0004-6361/201322100

Corsali, A. 1516, Lettera allo Illustrissimo Signore Duca Giuliano de' Medici (1517 manuscript), Digital reproduction on Atlas Coelestis. `https://www.atlascoelestis.com/Corsali%20manoscritto%201517.htm`

de los Reyes, M. 2023, Physics Online Journal, 16, 152, doi: `10.1103/Physics.16.152`

de Vaucouleurs, G. 1955, *The Astronomical Journal*, 60, 126, doi: `10.1086/107173`

de Vaucouleurs, G., & Freeman, K. C. 1972, Vistas in Astronomy, 14, 163, doi: `10.1016/0083-6656(72)90026-8`

Dennefeld, M. 2020, The Messenger, 181, 37, doi: `10.18727/0722-6691/5210`

Dieter, N. H. 1965, *The Astronomical Journal*, 70, 552, doi: `10.1086/109780`

D'Onghia, E., & Fox, A. J. 2016, , 54, 363, doi: `10.1146/annurev-astro-081915-023251`

Dopita, M. A., Mathewson, D. S., & Ford, V. L. 1985, *The Astrophysical Journal*, 297, 599, doi: `10.1086/163556`

El Youssoufi, D., Cioni, M.-R. L., Bell, C. P. M., et al. 2019, *Monthly Notices of the Royal Astronomical Society*, 490, 1076, doi: `10.1093/mnras/stz2400`

—. 2021, *Monthly Notices of the Royal Astronomical Society*, 505, 2020, doi: `10.1093/mnras/stab1075`

El Youssoufi, D., Cioni, M.-R. L., Kacharov, N., et al. 2023, *Monthly Notices of the Royal Astronomical Society*, 523, 347, doi: `10.1093/mnras/stad1339`

Emerson, J., McPherson, A., & Sutherland, W. 2006, The Messenger, 126, 41

Fabrizio, M., Nonino, M., Bono, G., et al. 2011, , 123, 384, doi: `10.1086/659743`

Gaia Collaboration, Luri, X., Chemin, L., et al. 2021, *Astronomy & Astrophysics*, 649, A7, doi: `10.1051/0004-6361/202039588`

Gonneau, A., Lyubenova, M., Lançon, A., et al. 2020, *Astronomy & Astrophysics*, 634, A133, doi: `10.1051/0004-6361/201936825`

Graczyk, D., Pietrzyński, G., Thompson, I. B., et al. 2020, *The Astrophysical Journal*, 904, 13, doi: `10.3847/1538-4357/abbb2b`

Harris, J. 2007, The Astrophysical Journal, 658, 345, doi: `10.1086/511816`

Harris, J., & Zaritsky, D. 2008, , 25, 116, doi: `10.1071/AS07037`

Herschel, Sir, J. F. W. 1847, Results of astronomical observations made during the years 1834, 5, 6, 7, 8, at the Cape of Good Hope; being the completion of a telescopic survey of the whole surface of the visible heavens, commenced in 1825

Hindman, J. V., Kerr, F. J., & McGee, R. X. 1963, Australian Journal of Physics, 16, 570, doi: 10.1071/PH630570

Ideler, L. 1806, Historical Investigations on the Astronomical Observations of the Ancients (Bavaria, Germany: Quien)

Katz, D., Sartoretti, P., Guerrier, A., et al. 2023, *Astronomy & Astrophysics*, 674, A5, doi: 10.1051/0004-6361/202244220

Koch, A., Grebel, E. K., Kleyna, J. T., et al. 2007, *The Astronomical Journal*, 133, 270, doi: 10.1086/509889

Lindegren, L., & Dravins, D. 2003, *Astronomy & Astrophysics*, 401, 1185, doi: 10.1051/0004-6361:20030181

Livanou, E., Gonidakis, I., Kontizas, E., et al. 2007, *The Astronomical Journal*, 133, 2179, doi: 10.1086/512768

Mackey, D., Koposov, S., Da Costa, G., et al. 2018, , 858, L21, doi: 10.3847/2041-8213/aac175

Mathewson, D. S., Cleary, M. N., & Murray, J. D. 1974, *The Astrophysical Journal*, 190, 291, doi: 10.1086/152875

McMahon, R. G., Banerji, M., Gonzalez, E., et al. 2013, The Messenger, 154, 35

—. 2021, VizieR Online Data Catalog: The VISTA Hemisphere Survey (VHS) catalog DR5 (McMahon+, 2020), VizieR On-line Data Catalog: II/367

Muraveva, T., Subramanian, S., Clementini, G., et al. 2018, *Monthly Notices of the Royal Astronomical Society*, 473, 3131, doi: 10.1093/mnras/stx2514

Pasquini, L., Avila, G., Allaert, E., et al. 2000, in Society of Photo-Optical Instrumentation Engineers (SPIE) Conference Series, Vol. 4008, Optical and IR Telescope Instrumentation and Detectors, ed. M. Iye & A. F. Moorwood, 129–140, doi: 10.1117/12.395491

Pasquini, L., Avila, G., Blecha, A., et al. 2002, The Messenger, 110, 1

Pietrzyński, G., Graczyk, D., Gallenne, A., et al. 2019, , 567, 200, doi: 10.1038/s41586-019-0999-4

Rathore, H., Besla, G., Daniel, K. J., & Beraldo e Silva, L. 2025a, *The Astrophysical Journal*, 988, 79, doi: 10.3847/1538-4357/ade0ae

Rathore, H., Choi, Y., Olsen, K. A. G., & Besla, G. 2025b, *The Astrophysical Journal*, 978, 55, doi: 10.3847/1538-4357/ad93ae

Ripepi, V., Chemin, L., Molinaro, R., et al. 2022, *Monthly Notices of the Royal Astronomical Society*, 512, 563, doi: 10.1093/mnras/stac595

Rubele, S., Pastorelli, G., Girardi, L., et al. 2018, *Monthly Notices of the Royal Astronomical Society*, 478, 5017, doi: 10.1093/mnras/sty1279

Ruiz-Lara, T., Gallart, C., Monelli, M., et al. 2020, *Astronomy & Astrophysics*, 639, L3, doi: 10.1051/0004-6361/202038392

Russell, S. C., & Dopita, M. A. 1992, *The Astrophysical Journal*, 384, 508, doi: 10.1086/170893

Skowron, D. M., Jacyszyn, A. M., Udalski, A., et al. 2014, *The Astrophysical Journal*, 795, 108, doi: 10.1088/0004-637X/795/2/108

Skrutskie, M. F., Cutri, R. M., Stiening, R., et al. 2006, *The Astronomical Journal*, 131, 1163, doi: 10.1086/498708

Stanimirović, S., Staveley-Smith, L., & Jones, P. A. 2004, *The Astrophysical Journal*, 604, 176, doi: 10.1086/381869

Subramaniam, A. 2003, , 598, L19, doi: 10.1086/380556

Subramaniam, A., & Subramanian, S. 2009, , 703, L37, doi: 10.1088/0004-637X/703/1/L37

Sutherland, W., Emerson, J., Dalton, G., et al. 2015, *Astronomy & Astrophysics*, 575, A25, doi: 10.1051/0004-6361/201424973

Taylor, M. 2011, TOPCAT: Tool for OPerations on Catalogues And Tables, Astrophysics Source Code Library, record ascl:1101.010. http://ascl.net/1101.010

van den Bergh, S. 2000, The Galaxies of the Local Group

van der Marel, R. P. 2006, in The Local Group as an Astrophysical Laboratory, ed. M. Livio & T. M. Brown, Vol. 17, 47–71, doi: 10.48550/arXiv.astro-ph/0404192

van der Marel, R. P., & Cioni, M.-R. L. 2001, The Astronomical Journal, 122, 1807

Watkins, L. L., van der Marel, R. P., & Bennet, P. 2024, *The Astrophysical Journal*, 963, 84, doi: 10.3847/1538-4357/ad1f58

Westerlund, B. E. 1997, The Magellanic Clouds

Appendix A

Stellar populations

This appendix provides supplementary material to Chapter 4. Table A.1 lists the boundaries of the CMD regions used in the stellar population analysis, while Figures A.1–A.5 show the radial velocity distributions and velocity-coded spatial maps for all regions discussed in Section 4.3.

Table A.1: Regions in the $(J - K_s, K_s)$ CMD used in this work, defined based on Cioni et al. (2014) and modified as in El Youssoufi et al. (2019). The boundaries depend on both the color J-K$_S$ and the magnitude K$_S$.

Region	Range
A	$-0.2 < J - K_s < 0$; $10 < K_s < 16.5$
	$K_s < -25(J - K_s) + 16.5$
B	$K_s < 19$; $-25(J - K_s) + 16.5 < K_s < -13.33(J - K_s) + 19$
	$K_s > 3.33(J - K_s) + 16.5$
C	$K_s < 19$; $-13.33(J - K_s) + 19 < K_s < -6(J - K_s) + 19.9$
	$K_s > 2(J - K_s) + 16.7$
D	$K_s < 19$; $-6(J - K_s) + 19.9 < K_s < -15(J - K_s) + 25$
	$K_s > -2.5(J - K_s) + 18.5$
E	$16 < K_s < 19$
	$-30(J - K_s) + 37 > K_s > -15(J - K_s) + 25$
F	$J - K_s < 0.9$; $K_s < 19$
	$K_s > -30(J - K_s) + 37$; $K_s > -8.75(J - K_s) + 22.125$
G	$0 < J - K_s < 0.2$
	$10 < K_s < 16$
H	$J - K_s > 0.2$; $10 < K_s < 16$
	$K_s < -15(J - K_s) + 22$
I	$J - K_s > 0.4$; $K_s > 10$
	$-15(J - K_s) + 22 < K_s < -9.17(J - K_s) + 20.92$
J	$J - K_s > 0.4$
	$-9.17(J - K_s) + 20.92 < K_s < -2.5(J - K_s) + 18.5$
K	$12.5 < K_s < 16$
	$-15(J - K_s) + 25 < K_s < -8.75(J - K_s) + 22.125$
L	$0.9 < J - K_s < 2.2$; $12.5 < K_s < 19$
	$K_s > -8.75(J - K_s) + 22.125$
M	$0.9 < J - K_s < 1.5$
	$10 < K_s < 14$

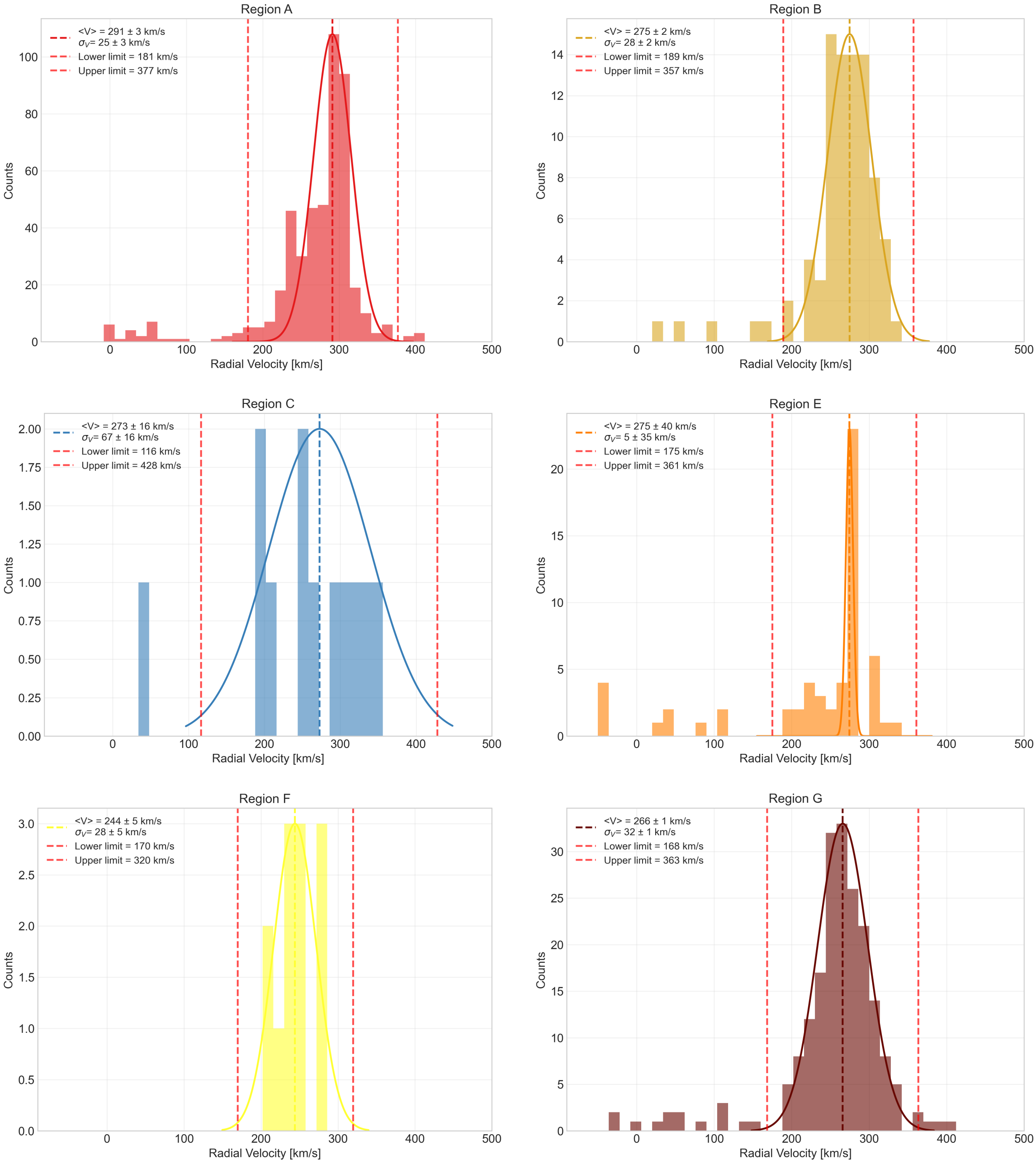

Figure A.1: Radial velocity distributions for stars in Regions A-G, with a bin size of 14 km s^{-1}. Region D is excluded due to insufficient statistics (N = 3). Each panel shows the velocity histogram for one region, with the Gaussian fit overlaid as a colored curve and the mean RV indicated by the matching color dashed line. The two red dashed lines represent $\pm 3\sigma$ selection limits used to define the LMC membership. Note the non-Gaussian distribution of Region E, already shown in Fig. 4.10.

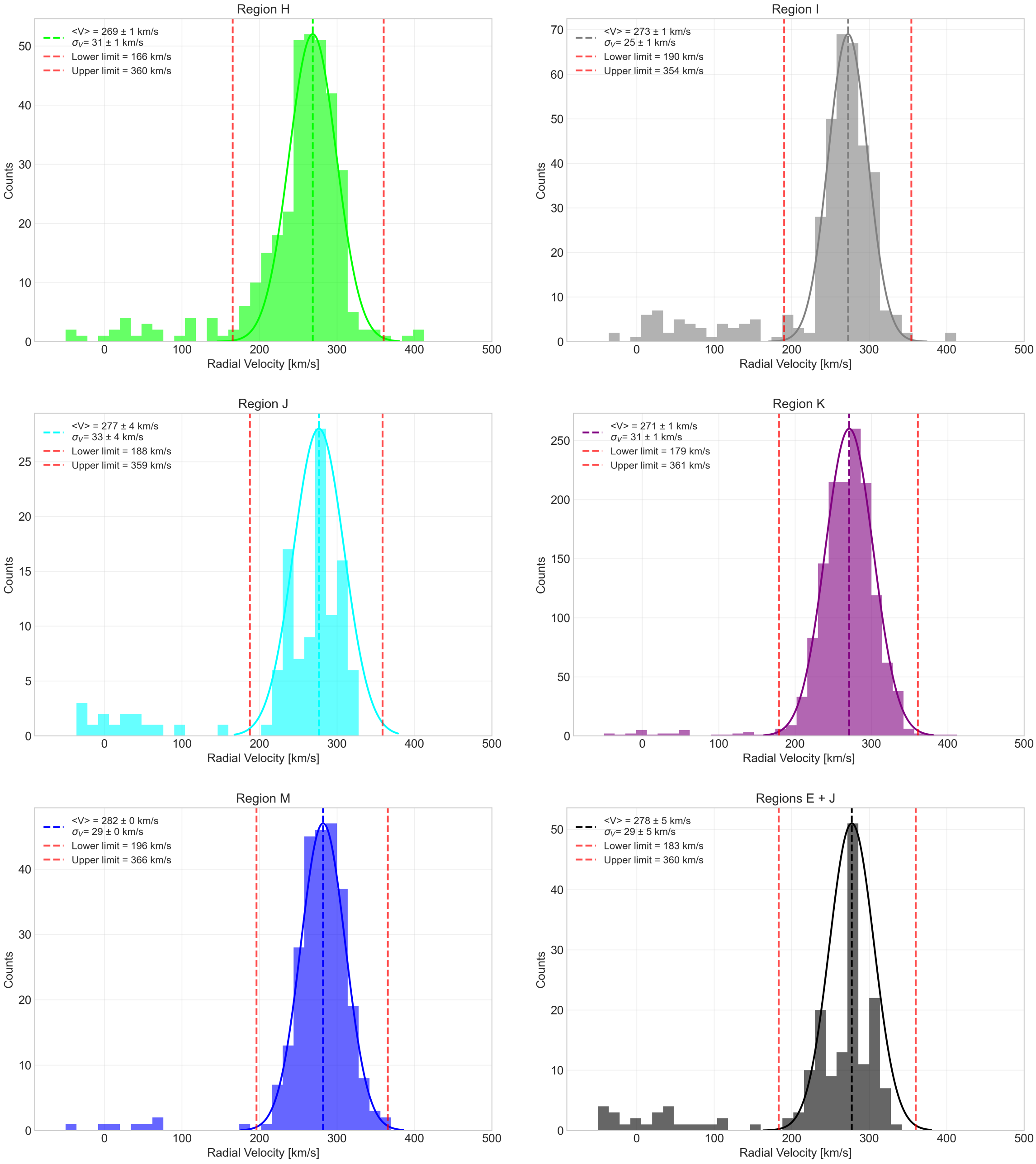

Figure A.2: Same as A.1, but for Regions H-M and the combined Region E+J, where merging the two regions results in a distribution closer to a Gaussian profile and significantly reduced uncertainties compared to Region E alone. Region L is excluded because it is populated mostly by foreground galaxies.

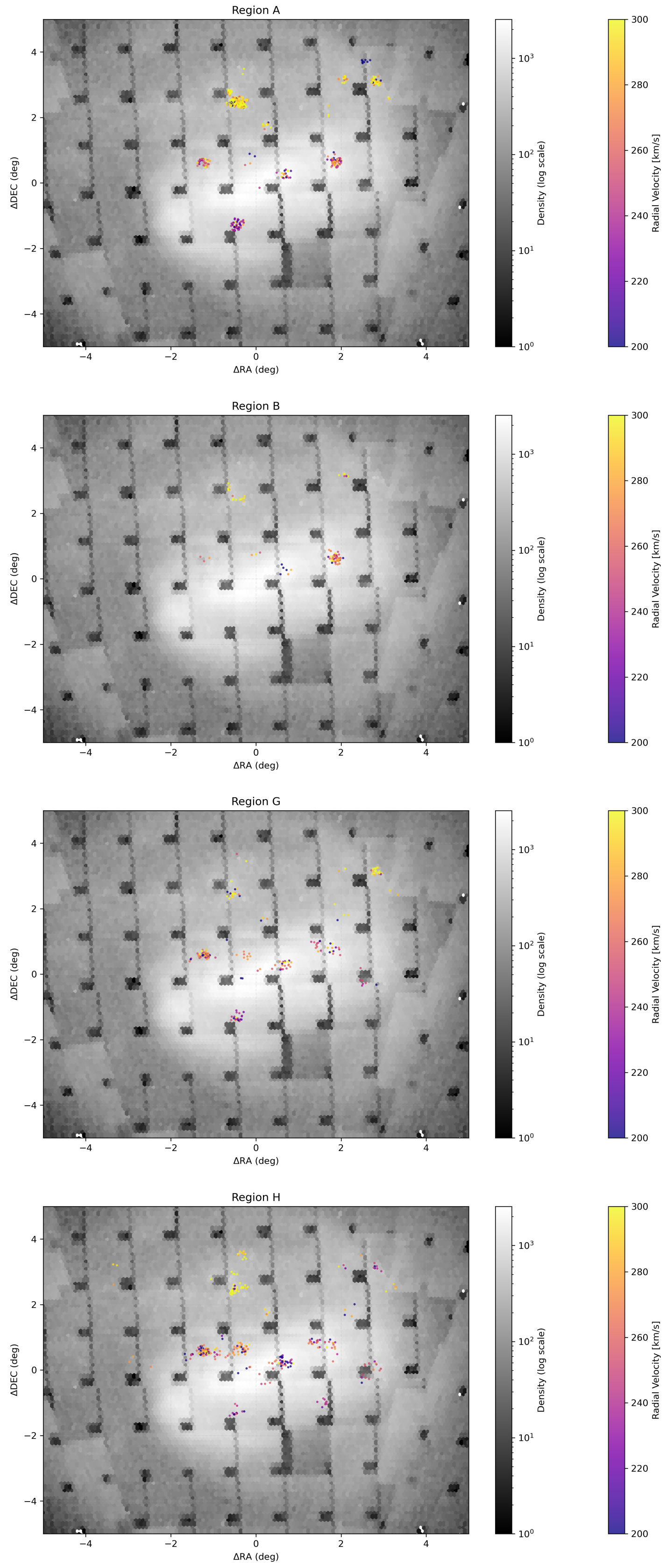

Figure A.3: RV-coded spatial distribution maps for Regions A, B, G, and H. Each panel shows the positions of stars in a given region in the deprojected ΔRA–ΔDec plane, within a range of −5° to 5° in both axes, color-coded according to their radial velocity following the same color scale used in the main text. The gray-scaled background shows the full photometric sample, with lighter shades indicating higher stellar density on a logarithmic scale.

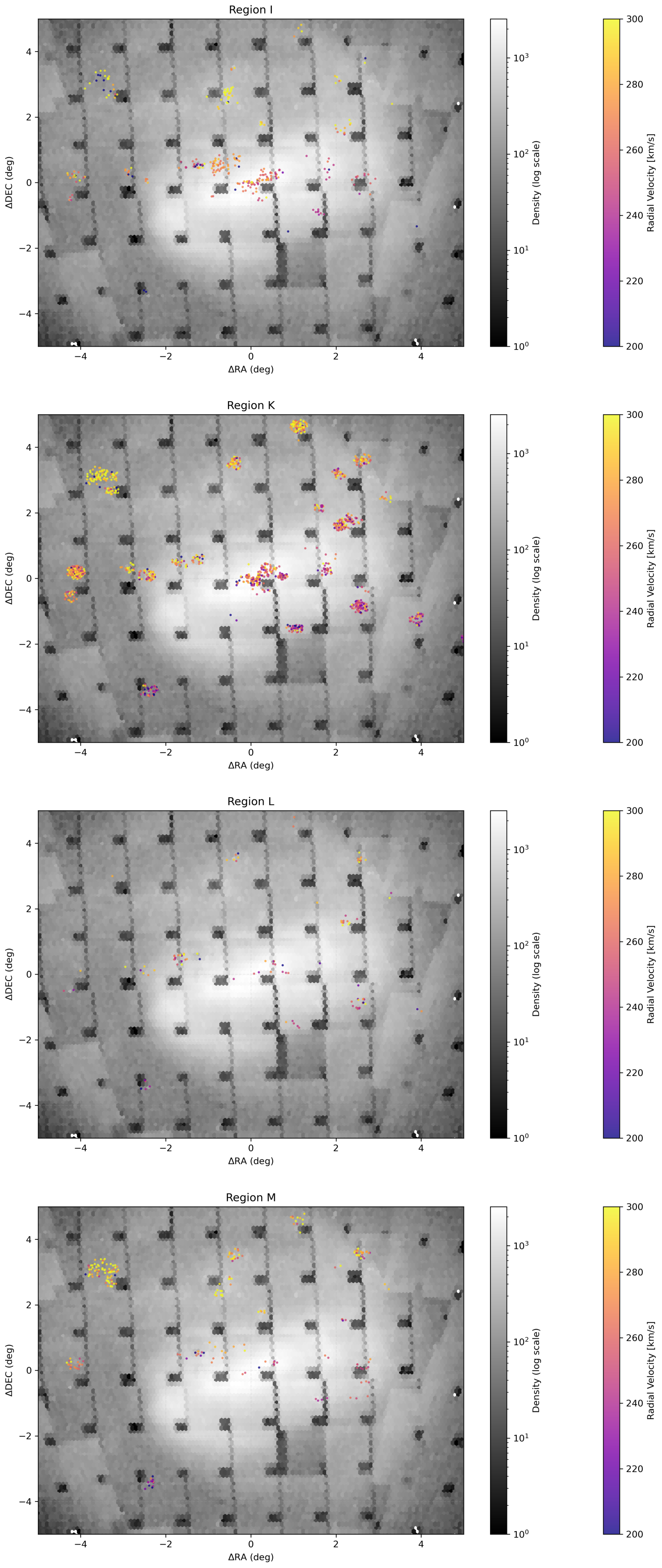

Figure A.4: Same as Fig. A.3, but for Regions I, K, L, and M.

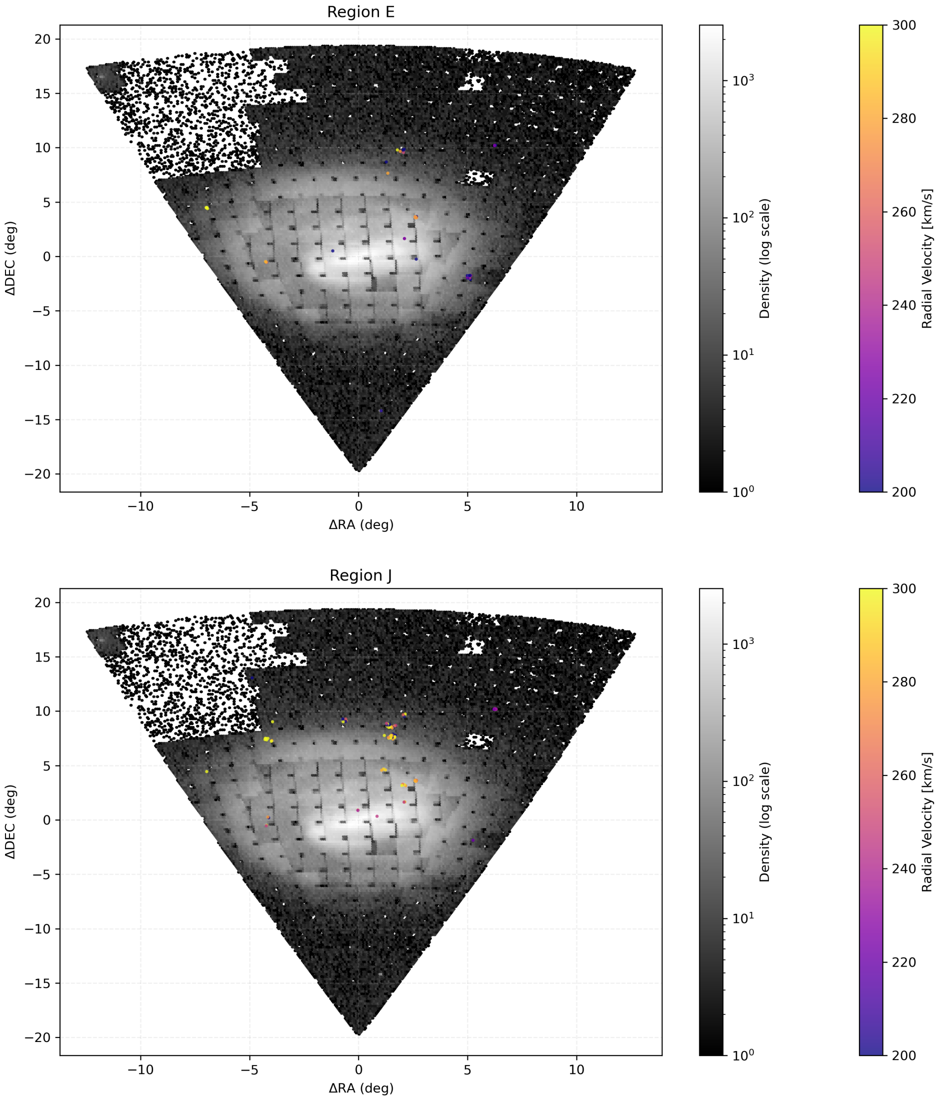

Figure A.5: RV-coded spatial distribution maps for Regions E and J. Same as Figure A.3, but showing the full field of view, as these populations are more spatially extended and less concentrated toward the center of the LMC.